An Investigation into the use of a Mis-Tuned Rotor for Measurement of Pressure Distortion during Wind Tunnel Inlet Integration Tests

A Thesis Presented for the

Master of Science

Degree

The University of Tennessee, Knoxville

Stephen Andrew Arnold

December 2018

DEDCIATION

To my mother

Jane Arnold,

My father

Bill Arnold,

And my brother

John Arnold.

ACKNOWLEDGEMENTS

I would like to express my deep gratitude to Dr. Phuriwat Anusonti-Inthra and Dr. Reza Abedi for advising this work over many years. The patience and support that my thesis committee, Dr. Monty Smith and Dr. Greg Power, showed was also greatly appreciated. Thank you to my many managers and mentors over the years (Jim Davis, Rob McCamis, Ed Wantland, Mark Chappell, and Mark Bymaster) that continued to push me to make progress on my graduate studies when I needed the motivation. Joel Davenport, Jonathan Kolwyck, and Andrew Davis provided many hours of test support at UTSI and were always accommodating of my requests. Much of the work presented was built on the talents of Justin Garrard, Bryan Hayes, Terry Hayes, Rylan Cox, Nathan Harrison, and Tom Tibbals who assisted with the test rig and the NSMS. Thank you to Kurt Nichol from Apex Turbine Testing for providing measurement hardware and software used to acquire the data for this thesis. Many thanks also to the others at UTSI, ATA, QuantiTech, and the United States Air Force that have helped in countless other ways.

Most of all I would like to thank my wife Kim Arnold and our children Katherine and Lauren for their encouragement for me to continue and their understanding for my absences.

ABSTRACT

During the development of modern aircraft, testing of sub scale models of the airframe is often done in wind tunnels to evaluate the effect that the aircraft inlet can have on the propulsion system. During these inlet integration test, special test equipment is required to vary the airflow through subscale inlet to represent an engine that varies from low to high thrust levels. A forty pressure probe array is also frequently used to characterize potential pressure defects in terms of extent (angular range of low pressure defect) and intensity. This thesis explores using a rotor with blades of different modal frequencies (mis-tuned rotor) to both vary the airflow through the inlet and measure the pressure distortion extent and intensity. The pressure distortion extent and intensity is determined by measuring blade vibrations using a Non-intrusive Stress Measurement System (NSMS). The blade vibrations are an input to an algorithm that evaluates the Fourier series composition of the circumferential pressure variation.

An experimental rig with a mis-tuned rotor was developed to explore the new measurement device. Variations in blade vibratory amplitudes with varying pressure distortion levels were measured with the experimental rig, but blade excitation from other experimental rig features limited the usability of the test results. An effort was then undertaken to develop a model in the Simulink® environment that matched the experimental test rig results. This simulation did

match the experiment rig results, and final evaluation of the proposed device was performed using the simulation alone.

The measurement device as proposed in this thesis was limited to measuring pressure distortion with the desired uncertainty requirements at only one airflow. Recommendations are made to reconfigure the mis-tuned rotor to permit measuring pressure distortion at up to four different airflows. Recommendations are also made for advanced NSMS processing algorithms that will result in a reduction in the pressure measurement error.

TABLE OF CONTENTS

LIST OF TABLES

LIST OF FIGURES

LIST OF NOMENCLATURE AND SYMBOLS

2E, 3E, etc	2nd Engine Order, 3rd Engine Order, etc
AIP	Aerodynamic Interface Plane
a_n	Coefficient of cosine term ‘n’ of Fourier Series
b_n	Coefficient of sine term ‘n’ of Fourier Series
ARP	Aerospace Recommended Practice
BTT	Blade Tip Timing
c	Damping
c_c	Critical Damping
CFD	Computational Fluid Dynamics
COTS	Commercial off the Shelf
DPCQP	Distortion Intensity – Delta Pressure Circumferential / Pressure
E	Engine Order
EDAS	Experimental Design and Analysis Solutions
EO	Engine Order
EXT	Distortion Extent
f	Frequency
FEM	Finite Element Method
GTE	Gas Turbine Engine
H_{EXT}	Harmonic Coefficient as a function of Extent
H_{MAX}	Maximum Value of Harmonic Coefficient
HWB	Hybrid Wing Body

k	Stiffness
LED	Light Emitting Diode
m	Mass
n	Fourier Series harmonic number
N	Rotor Speed
NASA	National Space and Aerospace Administration
NFAC	National Full-Scale Aerodynamic Complex
NSMS	Non-contact Stress Measurement System
PAV	Average Pressure
PAVLOW	Average Pressure, Low Pressure Region
PDS	Probe Difference Scalar
SAE	Society of Automotive Engineers
TDC	Top Dead Center
TECT	Turbine Engine Component Testbed
TOA	Time of Arrival
TPS	Turbine Powered Simulator
x	Displacement
θ	Circumferential Location
ω_n	Natural Frequency
ζ	Damping Ratio
Ω	Frequency Ratio
Φ	Phase Difference between Input and Output

CHAPTER ONE

INTRODUCTION AND GENERAL INFORMATION

The design of modern aircraft requires consideration of how the propulsion system and associated inlet will be integrated with the airframe. Testing is often conducted in a wind tunnel with heavily instrumented scale models to ensure the integrated aircraft and propulsion system provides the overall desired performance when the system is fielded. An example of a recent test where airframe effects on propulsion system performance were investigated in a wind tunnel is shown in Figure 1 (Figures are included in the Appendix).   This test was performed by the National Aeronautics and Space Administration (NASA) to evaluate a Hybrid Wing Body (HWB) scale model in the National Full-Scale Aerodynamic Complex (NFAC) wind tunnel in California[1].   The two nacelles for directing flow to the turbine engine-based propulsion system are highlighted at the top rear portion of the HWB model.

A feature that is different for the HWB compared to many present-day aircraft are the inlets for the two turbine engine propulsion systems are above the airframe near the back end of the HWB. Many present-day aircraft have the engines mounted under wing with the nacelle inlets that provide airflow to the engine located forward of the wing leading edge. The potential that flow going into the engine inlets of the HWB would be significantly affected by flow across the body was a primary consideration for this test. The test setup also included additional hardware at the back of the model (Figure 2) to control the mass flow through the engine nacelles during the test with an ejector system. Additional detail of the flow path through the nacelle and ejector is shown in Figure 3.

During wind tunnel inlet integration tests, not only is additional test equipment required to control mass flow through engine nacelles as shown in Figure 3, but typically additional instrumentation is required to characterize inlet flow characteristics. Figure 4 provides detail on the inlet instrumentation rakes that were installed for the HWB model test. The 40 probe survey from eight rakes mounted in the right inlet (Figure 4b) is a common configuration used in inlet integration test to measure the pressure field with industry stand techniques described later in this thesis.

The data collected from the pressure measurements acquired in a wind tunnel test can be used to evaluate three different potential influences on the engine. First, an estimate of the inlet effect on engine performance is frequently evaluated by determining the average total pressure at the inlet of the nacelle compared to the average total pressure at the engine face. This relation between inlet of the nacelle and engine face pressure is defined as inlet recovery. Second, the spatial variation of the pressure measured at different locations within the measurement array is critical to understand the influence on engine compressor stall characteristics. More detail for the pressure spatial variation characterization is provided later in the thesis. A third consideration of the effect of inlet flow characteristics on the engine is the compressor blade vibrations that might be excited by non-uniformity in the inlet flow. This Aeromechanical consideration is often computationally intensive and requires the additional use of Computational Fluid Dynamics (CFD) and structural Finite Element Method (FEM) models to understand the inlet effects.

Because of the expenses that can be incurred for a complex inlet integration test, test time can be limited. Additionally, some facilities, such as academic institutions or small businesses, might not have the resources available to perform test with large channel count instrumentation configurations and significant additional test equipment such as the mass flow control ejector. This thesis explored taking advantage of recent technology trends to develop a measurement and metering device that could potentially reduce the cost of wind tunnel inlet integration tests. The device considered was a rotor with blades that have different natural frequencies (mis-tuned rotor) that are excited by pressure disturbances in the inlet. The mis-tuned rotor could be driven by a commercial off the shelf (COTS) variable speed electric motor to meter the flow. The benefits considered for this approach are a reduction in the total measurements and a reduction in size of the airflow metering hardware. Another benefit considered for this device is direct measurement of Aeromechanical forcing from the pressure field on rotating blades instead of the approaches that require the use of CFD or FEM models. Table 1 (included in the Appendix) provides a comparison between current legacy technique features and the goals of the proposed technique.

It is realized that the new device as proposed would have some unfavorable characteristics compared to traditional approaches for inlet integration tests. Measurement uncertainty with the new device would be greater than with a 40-probe array as shown in Figure 4b. Another disadvantage of the mis-tuned rotor compared to traditional inlet integration test techniques is that only three to six airflows can be evaluated at specific rotor speeds of the device. Traditional airflow metering hardware, such as the ejectors, have a much wider range of airflow settings. Despite these limitations, the intent for the developing the new pressure distortion measuring device was to provide users an option for the situations when measurement uncertainty requirements can be relaxed when limited resources and time are available.

An experimental rig was initially used to evaluate the proposed measurement device, and final evaluations were made using simulations. The simulations indicate the measurement uncertainty goals could be achieved with some additional optimization beyond the work described in this thesis.

CHAPTER TWO

WIND TUNNEL INLET INTEGRATION TESTS

Types of Wind Tunnel Tests

Since the initial days of heavier-than-air flight, sub-scale testing of aircraft designs in wind tunnels has proven to be an effective method to understand the aerodynamics and forces that can be expected on full scale airframes. The Wright Brothers were one of the early pioneers of flight that learned that wind tunnels could provide crucial information that was not available from other sources in the design of aircraft. Because their initial attempts at aircraft design resulted in aircraft that only produced one third of the expected lift[2], they built a wind tunnel to obtain measurements of lift and drag of sub-scale airfoils. With this data obtained from the wind tunnel, they were able to make modifications to their aircraft designs and were not subjected to such drastic surprises during subsequent flights.

As time and aircraft designs have progressed, the types of test and information that can be obtained from a sub-scale wind tunnel test has also expanded. Some of the different types of tests that can be conducted in present day Wind Tunnels are listed below:

1. Aerodynamic Performance with Force Measurement[3]: These tests include mounting the model in such a manner that all three forces and moments created by the airframe can be measured and are similar to

original tests conducted by the Wright brothers. Typically, the model can be set to different angles of attack (alpha) or sideslip (beta) relative to the flow field. These tests may include the ability to vary control surfaces to determine the effect on aerodynamic forces.

2. Flow Field Characterization with Pressure Measurements[4]: These tests are often conducted when the aircraft configuration is near final. These tests have increased pressure measurements to obtain detailed load information for structural design, determine points on the airframe that have critical flows when traversing sonic velocity, and fast response pressures to evaluate the potential of buffeting.
3. Store Separations Tests[5]: For military aircraft, these tests evaluate aerodynamic characteristics of stores on the aircraft that will separate during flight. The stores include external fuel tanks and other weapons that will be launched from the aircraft. These tests ensure that when the store separates from the aircraft it will do so in a stable manner.
4. Jet Effects Tests[6]: These tests evaluate the effect of high velocity jets leaving the propulsion system through exhaust nozzles. These tests often require a separate high-pressure source to create the flow through the exhaust nozzle at the correct simulated pressures and Mach numbers.
5. Inlet Integration Tests[7,8]: These tests attempt to determine how a propulsion system (often a turbine engine) can be integrated with the

airframe and the resultant effects each might have on the other. In particular, for military aircraft that often undertake extreme maneuvers at large angles of attack or sideslip, the air flowing into the propulsion system inlet is often blocked or disturbed. This results in non-uniformity of the pressure field at the engine face (distortion) that potentially could affect engine operation or durability.

6. Turbine Powered Simulator (TPS) Test[9,10]: While a Jet Effects test evaluates the exhaust characteristics of a propulsion system on an airframe, and an Inlet Integration tests evaluates the inlet characteristics, a Turbine Powered Simulator test uses a sub-scale compressor and turbine to represent the engine and study both inlet and nozzle effects at the same time. Often the details of the turbine engine are not defined well enough during the wind tunnel test to build a sub-scale version that is adequate for the inlet and jet effects evaluation.

Pressure Measurement for Inlet Integration Tests

By the 1960's, aircraft and turbine engine design organizations realized an improved method was needed to define how aircraft inlet behavior influenced engine operation. In 1972, the Society of Automotive Engineers (SAE) Aerospace Council Division Technical Committee S-16 was formed to review aircraft inlet/gas turbine engine interface flow field interactions[7]. The SAE S-16 committee defined relevant parameters that could be used as airframe manufacturers worked with engine manufacturers to improve the integration process. In March of 1978 the S-16 committee released Aerospace Recommended Practice ARP1420 “Gas Turbine Engine Inlet Flow Distortion Guidelines”[8]. This document provided recommendations for measurement and evaluation of the total pressure field at the interface between the aircraft and the engine, defined as the Aerodynamic Interface Plane (AIP). This information was primarily used to evaluate engine performance and stability characteristics in the presence of these pressure fields.

ARP 1420 recommended that the total pressure field at the AIP be characterized with 40 total pressure measurements acquired at eight equal angle spaced rakes with five different radial locations. Figure **5** represents the configuration of pressure measurements recommended.

These pressure measurements can be made in the wind tunnel during sub-scale inlet integration tests. The data collected from the wind tunnel can be used later when performing full scale engine testing on ground test stands. Distortion descriptors are used to describe the pressure distortion measured with the 40 pressure measurements. The descriptors are classified as circumferential or radial. Figure 6 represents how the pressure measurement might vary around the circumference at a given radial location. The circumferential distortion descriptors are defined as intensity, extent, and multiple-per-revolution elements.

Circumferential distortion intensity defines the pressure defect that is measured at each radial circumference compared to the average pressure. This defect is defined by comparing the average pressure (PAV) at the location to the pressure in the low-pressure region (PAVLOW). As defined within ARP1420, circumferential distortion intensity (DPCQP) is:

$$DPCQP = \frac{(PAV - PAVLOW)}{PAV}$$

Equation 1.

Circumferential distortion extent defines the arc over which the pressure defect occurs. As defined within ARP1420, circumferential distortion extent (EXT) is:

$$EXT = \theta_2 - \theta_1$$

Equation 2.

There are other distortion descriptors defined by ARP1420, such as radial distortion intensity and Multi-per-Rev content that are beyond the scope of this thesis. ARP 1420 indicates that circumferential distortion intensity and extent should be calculated for each ring. For the purposes of this thesis, it was considered useful information to have an average circumferential intensity and average extent for the entire AIP. Because this thesis presents potential low-cost alternatives for measurement techniques during inlet integration tests, understanding if distortion was present or not and to what level was considered useful in the evaluation of inlet design characteristics.

Fourier Analysis of Once Per Rev Distortion

Though multi-per-rev distortion patterns are recognized as occurring in aircraft inlets and effecting turbine engine operation, for the purposes of this thesis, the simplest case of a once-per-rev pattern was the primary focus. For a pressure distortion pattern that is similar from one engine revolution to the next, a periodic characteristic can be considered. This periodic signal can be analyzed using a Fourier series. The generalized Fourier series for a periodic function over the interval from *-L* to *+L* is[13]

$$f(x) = a_0/2 + \sum_{n=1}^{\infty}\left(a_n \cos\frac{n\pi x}{L} + b_n \sin\frac{n\pi x}{L}\right)$$

Equation 3.

where;

$$a_0 = \frac{1}{L}\int_{-L}^{+L} f(x)dx$$

$$a_n = \frac{1}{L}\int_{-L}^{+L} f(x)\cos\frac{n\pi x}{L}dx$$

$$b_n = \frac{1}{L}\int_{-L}^{+L} f(x)\sin\frac{n\pi x}{L}dx$$

Equation 4.

for n = 1, 2, 3, etc. One classic example frequently evaluated with the Fourier series is a period square wave that has step changes in level over one half of the period from -L to +L with L = π. The Fourier series for the square wave is[14]:

$$f(x) = \frac{4}{\pi} \sum_{n=1,3,5,\ldots}^{\infty} \frac{1}{n} \left(\sin \frac{n\pi x}{L} \right)$$

Equation 5.

Where only odd values of n contribute in the combined signal. Figure 7 displays construction of the square wave and then additional contributions of n=1, n=1,3, n=1,3,5, etc.

This example of a square wave is symmetric with the same interval of +1 and -1 amplitude occurring over the period. In description of square waves, this characteristic is often described as a “50 % Duty Cycle”, where the higher level occurs over 50 % of the period. For the ARP 1420 descriptors defined previously, the square wave with the 50 % duty cycle can be considered to have an extent of 180°.

As shown by Equation 5, the coefficients for the square wave were defined as 4/(π*n) for the case with the 180° extent as defined by ARP 1420. To transition from the mathematical descriptors to the application of this thesis, the coefficients ‘n’ will also be described as ‘harmonics’ or ‘Engine Orders’. Also for this thesis, a simplifying assumption was made that the once-per-revolution pressure distortion pattern that would be measured would be a square wave that would have varying extent (or duty cycle).

Square waves of similar amplitude and varying extent were generated using a computer algorithm to determine how the coefficients would vary for the different harmonics (values of ‘n’). The square waves were evaluated using a Fourier Transform available in MATLAB to determine the contribution of each harmonic for the different extents[15]. Figure 8 displays the resultant Fourier series magnitude for different extents and harmonics (n).

From a review of these coefficients, patterns were recognized and could be used later in the evaluation of experimental results. The first characteristic was the maximum value of the harmonic coefficient (H_{max}) for any value of n and any extent could be defined by:

$$H_{max} = \frac{4}{\pi\, n}$$

Equation 6.

Analysis of the square wave with the 180 degree extent provided the coefficients for all the odd values of ‘n’, but it was apparent that the same relation bound the maximum value for the even values of ‘*n*’ as well.

Another characteristic revealed from review of Figure 8 was the feature that the coefficient went to zero at extents intervals equal to 360/n. For example, for a value of ‘n=2’, the function went to zero at an extent of 180 degrees. For a value of ‘n=3’, the function went to zero at an extent of 120 degrees. Based on review of these features, a generalized function that could be used to determine the harmonic coefficients for any square wave at any extent was defined as shown below:

$$H_{EXT} = \frac{4}{\pi\, n} * abs(\sin(Extent * n/2))$$

Equation 7

This relation shown in Equation 7 was used to provide a simple mechanism to evaluate experimental and simulation results described in subsequent sections.

CHAPTER THREE

BLADE VIBRATIONS, MIS-TUNED ROTORS, AND NSMS

Forced Response Blade Vibration

Understanding the vibratory characteristics of the turbine engine compressor blades is critical to provide a durable design that is not susceptible to fatigue cracking. The type of compressor blade vibrations might experience can categorized in to two primary areas. The most common blade vibration is known as a forced vibration driven by naturally occurring period excitation sources in the flow path. An example of a common source for blade excitation is shown in Figure 9[16]. A compressor stage consists of a rotating blade row followed by a stationary stator row. For a compressor with multiple stages, the alternating rotating blade row/stationary stator row results in multiple stages which all have different blade and stator counts. As the blades rotate through the flow path, variations in pressure downstream of the stators are periodic due to the symmetric nature of most stator vane assemblies. The periodic unsteady pressure imparted the rotating compressor blades is a naturally occurring excitation source for blade vibration.

The frequency of the excitation force on the rotating fan blades will be directly related to the number of stator vanes within the stage and the rotational speed of the compressor rotor. The common terminology used to define the number of stators in a stage that can generate an excitation is Engine Order

(EO). Because rotor speeds are typically defined as revolutions/minute and frequencies are typically defined in Hertz (cycles/second), the relation between the excitation frequency (f), rotor speed (N), and stator row count (EO) can be expressed mathematically as:

$$f = \frac{N(EO)}{60}$$

Equation 8.

The terms in this equation can be rearranged to calculate Engine Order if frequency and rotor speed are known by the following equation:

$$EO = \frac{60f}{N}$$

Equation 9.

The naturally occurring variable frequency excitation force present in the compressor results in a forced vibration that can be understood when considering a single-degree of freedom (SDOF) oscillator. For the SDOF oscillator under consideration, the parameters that effect the dynamic response to a periodic input are mass (m), damping (c), and stiffness (k). The system with an input force that is a function of time (F(t)) can be defined by the 2^{nd} order differential equation shown below:

$$F(t) = m\ddot{x} + c\dot{x} + kx$$

Equation 10.

Solving this 2^{nd} order differential equation yields parameters that are very useful in the definition of the vibratory characteristics of a spring-mass-damper system.

These parameters include the undamped natural frequency, ω_n , which is expressed in terms of mass and stiffness as

$$\omega_n = \sqrt{k/m}$$

Equation 11.

The critical damping, which is the level of damping that will prevent periodic motion from occurring in relation to mass and stiffness, is defined as:

$$c_c = 2\sqrt{mk}$$

Equation 12.

The critical damping ratio is defined as:

$$\zeta = c/c_c$$

Equation 13.

For the case where the excitation force, F(t), is a sinusoidal function of frequency, ω, the frequency ratio of exciting frequency to response frequency is defined as:

$$\Omega = \omega/\omega_n$$

Equation 14.

Defining the static displacement, X_{st}, as the displacement under the static load conditions of F/k, a dynamic amplification factor can be defined by the equation:

$$\frac{X\,(\Omega)}{X_{st}} = \frac{1}{\sqrt{(1-\Omega^2\,)^2 + (2\zeta\Omega)^2}}$$

Equation 15

Also, the angle Φ between the excitation force F(t) and the system response x(t) can be defined as:

$$\tan(\Phi) = \frac{c\omega}{k - m\omega^2}$$

Equation 16

Figure 10 displays the dynamic amplification factor and phase change that occur when the excitation frequency varies from less than to greater than the system natural frequency. The maximum amplitude of vibration occurs near the point where the frequency ratio is 1.

The characteristic amplitude and phase change shown in Figure 10 is present when rotor blades with a natural frequency are excited by passing through stator wake and bow wave disturbances. The blade forced response that occurs when the stator passing excitation frequency matches the blade modal natural frequency must be considered when designing turbine engines to be resistant to fatigue problems[17,18].

Though stators and struts can be inherent sources of excitation for turbine engine blades, other causes for forced response excitation can also occur once the engine is installed in an aircraft. One of the more widely recognized external sources of forced response excitation is from inlet pressure distortion[19,20]. The prediction methods prior to engine test and analysis methods after engine test, developed to understand the distortion driven blade forced responses, are the basis for much of the approach provided in this thesis.

Self-Excited (Flutter) Blade Vibrations

Another type of vibration that can occur in rotating blade row but is not as common as forced vibration is called a self-excited vibration. Self-excited vibration can occur without a naturally occurring excitation frequency present in the air stream. An example of this self-excited vibration can occur when the incidence angle on an airfoil increases to the point when stall is approached. The airfoil will deform as lift forces increase, but the airfoil will return to an undeformed position after lift forces are reduced at stall. An instability can arise where the change in aerodynamic forces will couple with the changes in displacement of the structure with varying load. As the aerodynamic fluid interacts with the structure and each affect the other, a dynamic instability can occur that is near a structural natural frequency. The case where the fluid-structure interaction occurs near the stall incidence angle of the blade is known as stall flutter[21,22,23]. Other types of self-excited vibration can occur within a compressor rotating blade row such as choked flutter[24]. This will occur at large negative incidences angles approaching the rotating blade row and is caused by shock waves that form and dissipate as the blade naturally deforms with varying load. Because of advancements in design practices learned through the years, self-excited vibrations such as stall flutter are less common in turbine engine compression systems than forced response vibrations. The self-excited vibrations can often be more damaging than forced responses however.

Mis-Tuned Rotors

The forced response characteristics defined for the SDOF system (equations 4 to 9) have proven to be of some use when evaluating turbine engine compressor blades. However, the true nature of the multi-degree of freedom blades and rotors can significantly deviate from the single degree of freedom assumptions under certain occurrences. Kielb[25], Besem[25], Castnier[26], and others[27] have observed that individual blades within a rotor stage can influence the vibratory characteristics of adjacent blades through both mechanical force transformation and disturbances to the air stream that occur during vibration. The characteristic that blades within a stage might have slightly different resonant frequencies for different modes of vibration has been defined as frequency mistuning. This frequency mistuning can occur due to manufacturing tolerances between blades during assembly, or from wear and tear on the blades during field service.

If the frequency variation between the blades for a given mode is large a rotor can be classified as a ‘mis-tuned’ rotor. Research by Castanier, Pierre, and others[28, 29] indicated that small levels of mistuning within a rotor system could result in amplification of the response amplitudes of the blades by a factor of 2 or more compared to a ‘tuned’ rotor. An example of increased amplitude for some mis-tuned rotors is shown in Figure 11.

Additional research by Castanier suggested that intentionally increasing frequency mis-tuning of a rotor beyond a critical value would eventually result in a reduction in the forced response amplitudes for a rotor stage. Similar research by Kielb and others[30] also indicated that intentional mistuning of a rotor blade stage could result in the increase in stall flutter margin (increased incidence angle prior to flutter) for a given blade row. The term ‘mis-tuned’ rotor is used to describe a compressor rotor that has blades with different vibratory frequencies for the same mode of vibration. The variation in frequency for the mis-tuned rotor build for this thesis is greater than the frequency variation used in modern compressor design practice to increase flutter margin.

Blade Vibration Measurement with NSMS

A Non-contact Stress Measurement System (NSMS) uses case mounted sensors to detect Time-of-Arrival (TOA) of blades near the sensor for calculation of blade deflection and vibration amplitudes[31, 32, 33]. NSMS, (also known as Blade Tip Timing or BTT) sensors are typically mounted on the case above the blades. Light is often projected from optical sensors into the blade passing channel and is reflected back to the probe. The reflected light then travels through a fiber optic connection to a point where the optical sensor is converted to an electrical signal with a photo-diode. As shown in Figure 12, precise electronic triggering circuits determine a TOA for each blade as it passes near the probe. A reference signal is typically mounted on the shaft to provide a rotational frame of reference for the period of the shaft rotation (1/Rev). Using simple assumptions about the radial location of the TOA measurements, a deflection of the blade can be calculated based on the blade tip velocities.

The blade arrival past the NSMS sensor will be ‘early’ or ‘late’ due to deformations. These deformations can be both ‘static’ deformations due to aerodynamic or centrifugal loading, or ‘dynamic’ deformations due to blade and shaft vibrations. Figure 13 is a representative NSMS measurement obtained from the test rig that highlight examples of both static and dynamic blade deflection characteristics as a function of rotor speed. For the two probes shown, static deflection due to aerodynamic and centrifugal load is apparent for the similar average increase in deflection with increasing rotor speed measured by both probes. Near 1600 RPM and 2800 RPM, dynamic deflections are measured with both probes as the blade pass through forced response that is an integral engine order. Because the vibration is an integer multiple of rotor speed, for the stationary probes on the case the deflection from one revolution to the next will not vary significantly from one revolution to the next. As a result, the probe will measure the blade at the approximate same location within the vibration cycle. The rise and fall of the deflection as the blade passes through the resonance with increasing speed is more apparent. This is due to the change in amplitude and phase that occurs with forced response as defined by Equation 15 (amplitude) and Equation 16 (phase).

Blade vibration amplitude is often the critical information needed from NSMS measurements. Hence a technique used to increase dynamic deflection while reducing the static deflection deformation, known as the probe difference, can be utilized. A probe difference will subtract the deflection measured on one revolution from one probe from another probe. Any common deflection to both probes will be removed. Because the static deformation is measured at similar amplitudes by all probes the primary deflection remaining will be the dynamic content.

The probe difference can also be used to increase the amplitude of the dynamic deflection. The increase in dynamic deflection amplitude is a function of the spacing of the two probes and the engine order of the blade vibration. This relation, known as Probe Difference Scalar (PDS), is shown below:

$$\mathrm{PDS} = 2 * abs(sin\frac{EO * (\theta_1 - \theta_2)}{2})$$

Equation 17

From equation 17, it is apparent that not only can a pair of probes be defined that can amplify the deflection measured by NSMS by a factor of 2.0 for a given engine order, but also a probe difference can be defined that will reduce the amplitude of a given engine order to near 0. Figure 14 displays the probe difference for the two probes shown in Figure 13. The characteristic of removing the static deflection is apparent and the amplification of the dynamic response amplitude due to vibration near 1600 RPM and 2800 RPM is also evident.

A simple method to determine the amplitude of vibration for the dynamic response measured by NSMS when passing through resonance is to subtract the minimum deflection measured by a probe difference from the maximum deflection. As shown in Figure 18, the amplitude measured by the NSMS probes for the response near 2800 RPM is 225 mils. Equation 18 defines how the NSMS probe difference relates to the deflection amplitude in peak-to-peak units:

$$\mathrm{Pk-Pk\ Deflection} = \frac{Probe\ Difference\ Amplitude * 2.0}{Probe\ Difference\ Scalar}$$

Equation 18

The maximum minus minimum probe difference calculation is a simple way to calculate deflection for the NSMS probe deflection, frequently used in the following sections. More advanced methods are available for processing NSMS data that provide more information besides the amplitude of vibration. Techniques are available to use non-linear least squares methods to solve Equations 15 and 16 to determine amplitude, resonant frequency, damping ratio, and phase from the deflection versus rotor speed data similar to that displayed in Figure 14. An example of this is shown in Figure 15, where commercially available software from Experimental Design and Analysis Solutions (EDAS)[34] used uses a Lavenburg-Marquedt least squares solver[35] to determine the critical parameters described.

This thesis researches the possibility of using a rotor that has intentional mis-tuning to measure the pressure variation of an inlet for a wind tunnel model. The mis-tuning for the different blades of the rotor is so that the blades would vibrate at the different frequencies but at the same rotor speed when excited by the pressure field. As defined by Equation 9, the frequencies would be at different integer Engine Orders (EO) for the same rotor speed. As the mis-tuned rotor speed was increased and decreased, the blade vibration levels were measured with NSMS. For example, at a given rotor speed, one group of blades might vibrate at the 2 EO frequency, another group of blades would vibrate at the 3 EO frequency, and so on. This information could be compared against theoretical frequencies from a Fourier analysis of a pressure field (Figure 8) to estimate the extent and intensity of the pressure distortion. This process of setting rotor speed of known resonance crossings of mis-tuned rotor, measuring blade vibration amplitudes with NSMS, and then calculating distortion extent and intensity is shown schematically in Figure 16.

CHAPTER FOUR

EXPERIMENTAL TEST AND SIMULATION DEVELOPMENT

Experimental Test Rig

The experimental fan rig used during for this research is part of the Turbine Engine Component Testbed (TECT) effort initiated by Aerospace Testing Alliance in 2014. The TECT test rigs provide hardware for experimentation of physical phenomena of interest in the development of turbine engines[36]. One of the TECT technology demonstrator rigs is a student designed ground-based gas turbine engine (GTE) with an augmenter. The compressor and turbine of the GTE, designated J1-H-01, is a T70 turbocharger that had an airflow of 1.4 pps and a compressor pressure ratio of 4.0. The combustor and augmenter for the GTE are constructed from student Josh Hartman's designs[37]. Figure 17 displays the turbocharger configured with the Hartman designed combustor. Figure 18 displays the TECT GTE in full augmentation.

Another test rig developed during the TECT initiative and used as a part of this research was a simple fan rig. The rig was designed to permit students to create simple Computational Fluid Dynamic (CFD) aerodynamic models and Finite Element Method (FEM) structural models for graduate level research[38]. The fan rig was based on a SpecrQuest™ Machine Fault simulator with a ½ HP electric motor. The single stage compression stage included six blades angled 45° relative to the centerline axis. The blades were made from simple flat aluminum sheet metal with the intention of varying the sheet metal thickness to vary blade natural frequencies and create a mis-tuned rotor. The simplicity of the geometry permitted rapid development of CFD and FEM models for predictions.

An emerging technology implemented to reduce the cost of fan rig construction was the use of a 3-D printer to construct aerodynamic surfaces of the fan rig. As shown in Figure 19, the nose cone (orange) at the entrance to the fan and the exit surfaces (red) covering shafts, bearings, and other potential obstructions were designed and constructed with the intent of providing uniform flow in and out of the fan similar to a turbine engine. The surfaces were manufactured using a MakerBot® Replicator 3-D printer. Another cost-saving construction technique implemented was the use of a cooking stock-pot with the bottom removed as the fan case.

To measure blade vibrations, a NSMS probe array was installed. The NSMS measurements were obtained using a beam interrupt probe with an Light Emitting Diode (LED) emitter at the entrance of the fan rig and an LED receiver at the exit of the fan rig (Figure 20). The mounts were constructed with the 3-D printer again to reduce cost. The use of an LED light sources resulted in a cost per probe of approximately $ 20 instead of the approximately $ 500 cost per Laser probe frequently used during turbine engine testing. To provide a mis-tuned rotor, the thickness of opposing blade pairs was varied by up to three different frequency blades per experiment. The blade thickness was limited to commercial-off-the shelf (COTS) aluminum sheet metal stock thicknesses.

. Other features of the aforementioned experimental rig were the five struts used to mount the inlet nose cone and the two support legs behind the rotating fan blades, which were used to mount the bearing support closest to the fan. These features are denoted in Figure 21. The significance of the struts and the bearing block supports is described in more detail in Chapter 5.

Another application of 3-D printing used for the construction of the experimental test rig was manufacture of distortion sectors of varying extent. Ferrer and Scheck[43] demonstrated the use of 3-D printing techniques to create distortion screens with complex total pressure patterns and swirl. The pressure distortion generated for this experiment was simple in comparison to the work of Ferrer and Scheck. The blockage contained a honeycomb pattern that included narrow passages to permit some flow to pass through. This resulted in a relative reduction in total pressure compared to the inlet area that did not contain the blockage. The construction of the sectors permitted experimental variation of the extent for this research. The blockage sectors were mounted to the struts that supported the nose cone at the inlet. To vary the intensity, layers of mesh fiber were attached to the front side of the distortion sectors to create increasing levels of airflow restriction and increasing distortion intensity.

To provide a mis-tuned rotor, the thickness of opposing blade pairs was varied to up to three different frequency blades per experiment. The opposing blade pairs must have the same thickness to maintain rotor balance. To minimize costs, the blade thickness was limited to COTS aluminum sheet metal stock thicknesses. The thicknesses tested were 1/32", 1/16", and 1/8". Important rig geometries and component details are provided in Table 2

Simulation

As described in subsequent sections, it became apparent that some type of modeling would be required to better understand unexpected results and to determine a path forward. The environment used for this model was Simulink®. Simulink® is a block diagram environment for multidomain simulation and Model-Based Design[45]. Simlulink® It is integrated with MATLAB to provide additional analysis capability of both the inputs and outputs for the models.

Figure 23 displays the block diagram model generated to represent the fan blade physics for the experimental rig. The block diagram is representative of the 2nd order differential equation shown in equation 10[46]. The block labeled "1/M" is for the forces generated as acceleration acts on the mass of the blade. The block labeled "b" represents the forces generated from when damping occurs at different blade velocities. The "b" terminology used for the simulation was equivalent to the "c" damping term of equation 10.. The block labeled "k" represents the forces generated from the stiffness of the blade that is deflected.

The input to the simulation was a time variant forcing function that was derived based on the analysis of experimental results. The time step could be varied to optimize the accuracy of the results with a manageable simulation time. The values for mass, damping, and stiffness were defined to match experimental results obtained with the fan rig described in later sections. MATLAB scripts were written to extract the equivalent NSMS data from the output files by extracting output values at the same equivalent angular position within the rotations that was comparable to the NSMS sensor locations. More detail on the simulation development and comparison to experiment results is described in Chapter 5.

CHAPTER FIVE

RESULTS AND DISCUSSION

Experimental Results

A test matrix was defined to generate a data set for verification of estimation of the pressure distortion extent and intensity. The test matrix consisted of slow fan rotor accelerations and decelerations without pressure blockages. This is installed to define a baseline of blade vibration for comparison with the different distortion blockage configurations. Testing would then continue with varying extents of blockage, intensity of blockage, and clocking relative to the fan case. Table 3 displays the first portion of the originally planned test matrix.

During the initial testing conducted it was apparent that the blade vibrations were greater than expected without any distortion blockage installed. An example of this is shown in Figure 19, with the NSMS measuring a blade vibration amplitude of 65 mils pk-pk for the 3E response at a rotor speed near 1650 RPM and an amplitude of 145 mils pk-pk for the 2E response at a rotor speed near 2850 RPM.

The test matrix was continued with the initial distortion blockages with the possibility that the baseline vibration amplitudes would be small compared to amplitudes generated with distortion. This would potentially enable ignoring the former part of amplitudes. Figure 25 displays the NSMS measurements from one blade acquired with the 90 % blockage installed at Top Dead Center (TDC – 0°). The dominant 2E response near 2850 RPM increased to 235 mils p-p compared to the 145 mils p-p measured without distortion (Figure 18). The 3E response near 1650 decreased compared to without distortion installed (45 mils vs. 65 mils).

Because of the presence of blade excitations without the distortion blockages installed, additional testing was defined to attempt to isolate the excitation source without distortion. The two physical obstructions closest to the rotating blades that might generate excitations were the five struts that held the nose cone in place and the two legs that held up the bearing block behind the blades (Figure 21). The influence of the five struts could be evaluated by removing them and the nose cone and repeating the acceleration/deceleration test. The two legs that held up the bearing block could not be removed and the distance between them and the rotating blades could not easily be altered. Potential excitation generated by the bearing block support legs could be altered by closing the space between the two legs. This was done using tape and the acceleration/deceleration test was repeated. It was noted that the vibratory response of the blades was significantly increased (Figure 26) compared to when the tape was not present (Figure 19). Table 4 through Table 6 display a summary of the average amplitude, frequency, and damping that were measured for the different hardware configurations tested to better understand influences of the hardware on blade excitation without the distortion blockage installed.

While work continued to better understand the results obtained with the nominal thickness blades the test rig was modified to the ‘mis-tuned’ configuration with three pairs of blades of different thicknesses. Figure 27 displays a representative data set collected for one of each of the three blade types: nominal, thin, and thick. The thickness of the blades (and the corresponding blade frequencies) were limited to common thicknesses available for sheet metal. It is apparent that the 2E and 3E responses occur at different rotor speeds as desired. Table 7 displays a summary of the resonant rotor speed and resonant frequency for the different resonant crossings measured with the different blade sets.

The data presented in Figure 27 and Table 7 indicate the blade frequency control available using the COTS aluminum sheet metal was not sufficient to build a mis-tuned rotor required for the proposed measurement device.

Simulation Development from Experimentation

Because there was only a small change in vibratory response when the five nose cone support struts were removed, attention was focused on determining a method to minimize the effect of the bearing block support legs. The initial method considered was modeling the combined effects of all excitation sources (distortion blockages, bearing block support legs, nose cone struts, etc.) using the Simulink® environment described earlier to potentially filter out the effects that were not of interest. The location of the excitations within a revolution were based on the angular range of the sources. Figure 28 displays a representation of the five nose cone struts and the two bearing block leg supports. Figure 29 displays an example of how the different elements were combined for the complex input for the simulation.

Based on data from turbine engine and fan tests, it is known that as rotor speed increases for a fan, the airflow and velocity into the rotor increase. Hence, it is expected that by increasing the velocities the excitation forces will increase correspondingly. To model this with the simulation, it was assumed that the excitation force amplitude would vary as a function of the square of rotor speed. This is represented in Figure 30 with both the input excitation and output response shown. This assumption appeared to be valid after comparing experimental and simulation results.

The simulation was exercised with varying elemental input combinations to attempt to replicate the results obtained during the experiments. An example of differences measured during the experiments that were matched with the simulation are shown in Figure 31 and Figure 32. Figure 31 displays the input signal and corresponding blade output for the case with the two bearing block supports providing the only excitation force. Figure 32 displays the case with the tape added between the two bearing block supports. The characteristic of significant increase in response amplitude with the addition of the tape was similar to results measured on the experimental test rig (Figure 19 and 21).

Through computational trial and error, additional relative input forces were defined for each excitation source exercised during the experimental phase. Simulations were run that combined each potential excitation source into one combined input signal. Table 8 through Table 10 display comparisons of amplitude measured during the experiments with amplitudes predicted from the simulation for the 2E, 3E, and 4E excitations. On average, the simulation amplitude was 0.5 % less than the experimental measurements.

From this analysis, it was apparent that using the simulation to remove blade excitations besides the blockage was beyond the scope of the thesis. Continued evaluation of the proposed measurement device required representative signals that would vary due to distortion only. Because of this, an approach was taken to use the simulation alone to understand the feasibility of using a mis-tuned rotor to measure pressure distortion and extent.

Simulation Results

After verifying that the simulation could represent the vibratory characteristics of the ‘nominal’ experimental blade set described above, additional simulation variables were created to represent a ‘mis-tuned’ rotor example. The design condition that was defined for modeling the mis-tuned rotor was the ‘nominal’ blade that had a 2E resonance near 2650 RPM rotor speed. This was slightly less than the ‘nominal’ frequency experimental blade that had a 2E resonance at 2850 RPM (Figure 19 and Figure 21).

Three different blade frequencies were available for the experimental mis-tuned rotor. However, it was considered that four different blade frequencies should be modeled on the simulated rotor to provide more opportunity for mutual resonant crossings for the different blades. At the design speed of 2650 RPM, the stiffness of the simulation was modified while maintaining mass and damping as a simple way to adjust the frequency. Besides the nominal blade that had a 2E resonance at 2650 RPM, other blades were modeled with reduced stiffness for a 1E resonant crossing at 2650 RPM and increased stiffness for 3E and 4E resonance at 2650 RPM. An example of the NSMS representation from the simulation output is shown in Figure 33.

The simulated mis-tuned rotor had the four initial rotor engine orders (1E, 2E, 3E, and 4E) at the design speed of 2650 RPM (Resonance Crossing 1). To permit estimation of extent and intensity at other corrected airflows, additional rotor speeds with more than one of the mis-tuned blade frequencies in resonance were identified. As shown in Figure 33, the 88 Hz blade and the 176 Hz blade both had a resonance at 1767 RPM (Resonance Crossing 2), and all four blades were in resonance at 1325 RPM (Half of the design speed – Resonance Crossing 3). Table 11 lists these resonant crossings and each mis-tuned blade set corresponding resonant Engine Order (E) crossing.

The simulations for the mis-tuned blades were performed using the increasing excitation as a function of rotor speed squared as shown in Figure 30.

The extent for the different simulation cases were performed as shown in

Table 12.

From the four NSMS probe locations that were simulated, a combination of probe differences that provided the maximum difference scalar were identified. These combinations provided the maximum NSMS deflection amplitude and reduced the extent and intensity calculation sensitivity to errors from all sources. Table 13 provides the list of probe combinations that provided the maximum NSMS difference scalar for each of the Engine Orders evaluated.

The outputs from the simulations were evaluated to calculate blade vibratory amplitude deflections measured with the NSMS probes for the probe combinations shown in Table 13. The simple maximum-minimum deflection through the resonance was used to define the amplitude of vibration. The results for Resonant Crossing 1 (2650 RPM) are shown in Table 14.

To compare amplitude ratios for the different blade frequencies for the mis-tuned rotor, corrections to the amplitude had to be made for stiffness of each blade and the NSMS difference scalar (Table 13). Table 15 displays the amplitudes that are corrected for the stiffness and NSMS probe combination differences. Similarly,

Table 16 and Table 17 display the adjusted amplitudes for the Resonant Crossing 2 and 3 rotor speeds, respectively.

With amplitudes available that can be compared against the theoretical excitation amplitudes shown in Figure 8, an algorithm was developed to calculate the sum of square errors between the NSMS determined amplitudes ratios and the theoretical amplitude ratios. The extent would then be defined as the angular position that had the minimum sum of the squares error. Figure 34 displays an example of the calculation of sum of square errors versus different potential extents for the simulation case where the actual extent was 100°.

Several features displayed on Figure 27 were also present at the other simulated cases as well. For the design speed (Crossing 1), there was only one minimum for all extents so that the estimated extent was always a single value. For Crossing 2, there were minimum values at 2 or 3 different extents. This was considered an artifact that at this crossing only two blades were vibrating, and the 6E engine orders was a multiple of the 3E engine order and not independent.

Figure 35 displays a comparison of the amplitude scalar for the 3E and 6E engine orders as a function of the extent for the two engine orders of rotor speed Crossing 2. This relation is defined in Equation 7. It is apparent that the amplitude relationship between the 3E and 6E excitation for 100° is the same as 20° and 140°. Likewise, for Crossing 3, typically two different extents would share the same local minimum value for the sum of the squares of the error. This was again considered to be caused by the fact that at the 1325 RPM crossing, the engine orders were all even numbered excitations, and therefore would be 'aliased' when attempting to determine the extent of the excitation. The need to consider the independence of the engine orders for the mis-tuned rotor is discussed further in Chapter 6.

Figure 36 displays the error in the calculated extent for the three different resonant crossing speeds. The goal was to be able to measure extent with an error of less than +/- 10°. At the design speed of 2650 RPM (Crossing 1), the only case in which calculation of the extent was not met was at the minimum extent (30°) and the error was 11°. As discussed earlier in this section, for the crossing 2 and 3 speeds, two or three extents were calculated based on 'aliasing' from the available engine orders because the engine orders were not optimized to determine the Fourier series coefficients. The data on the chart is shown for the calculated extent with the minimum angle to permit an analysis that could include a family of distortion characteristics when evaluating engine/inlet integration.

The +/-10° error target was not achieved for many of the Crossing 3 cases. These cases did not meet the target primarily because the blade vibration amplitudes were low for all of the blades at the test extent. An example of this is at an extent of 180°, the classical square wave case defined by equation 5. For this case only the odd engine orders (1E, 3E, 5E, etc) contribute to the periodic signal, while for Crossing 3 only even engine orders (2E, 4E, 6E, & 8E) were measured. The Crossing 3 result reveals that at least one blade that responds to an odd engine order excitation should be included in each crossing for the mis-tuned rotor. Additional discussion is provided in Chapter 6 related to recommendations for mis-tuning blade frequency characteristics that could reduce extent uncertainty.

Once an extent had been calculated from the NSMS amplitude measurements, the intensity could be calculated based on dividing the measured amplitude by the theoretical EO scalar shown in equation 4. Through review of the simulations, it was apparent that the error in intensity calculation could be reduced by using a weighted average from all available NSMS deflection measurements. For example, as shown in Table 18 for the 180° extent case, the 1E blade had a significantly higher amplitude than the next highest blade, the 3E blade. The 2E and 4E blade amplitudes were significantly less. This was expected for the classic square wave case (extent = 180°) that would contain only odd harmonics/engine orders. When an average that is weighted for the adjusted amplitude (2^{nd} column of Table 18), the calculated intensity (201.8 mils p-p) is within 1 % of the actual (203 mils p-p).

Figure 37 displays the error in intensity for the three different resonant crossing speeds as a function of extent. For the design speed (Crossing 1), the goal of +/- 5 % error was met for all extents above 45°. Part of the reason the intensity was calculated low for the 30° and 45° cases is the extent was calculated high. When the measured amplitude was adjusted for Fourier series scalar to determine intensity (Equation 7), the resultant amplitude would be too low. For Crossing 2 and 3, the intensity was calculated the same for all extents determined from the minimum sum of squares of the error (Figure 34).

The goal to define a mis-tuned rotor frequency combination that could achieve measurement uncertainty requirements for extent and intensity at three different rotor speeds was not achieved. Only the design speed (Crossing 1) achieved measurement uncertainty levels that were near the requirements. Chapter 6 discusses potential modifications that could be made to a mis-tuned rotor to provide improved measurement uncertainty results.

CHAPTER SIX

SUMMARY AND RECOMMENDATIONS

Summary

An investigation was undertaken to determine the feasibility of using a fan rotor with different resonant frequency blades (mis-tuned rotor) to measure spatial pressure variation in a wind tunnel model inlet. An experimental rig was built with a mis-tuned rotor and measurements were made with NSMS to evaluate the sensitivity to pressure distortion. This experimental rig did indicate the mis-tuned rotor blades were sensitive to pressure distortion but features of the experimental rig resulted in unanticipated blade vibrations that limited the usability of the test rig.

An additional effort was then undertaken to create a simulation of the test rig in Simulink® environment to understand the driving forces of the unanticipated blade vibrations for potential rig modification. This simulation provided insight to understand the excitation source for the blade vibrations (fan bearing block support struts), but the rig could not be modified to reduce the influence on the blade vibrations to an acceptable level. The simulation results were similar to experimental results for different non-distorted and distorted cases. Final evaluation of a proposed measurement device design was conducted using the simulation only.

The results of the analysis for the simulation indicated a mis-tuned rotor could be built that would measure the average intensity of a once-per-revolution distortion. The proposed device could measure pressure distortion at an uncertainty that is two to five times greater than the standard 40 pressure probe survey method. The extent of a once-per-revolution pressure distortion pattern could be determined within the goal of 10°. A limitation of the device as proposed was that only two or three corrected airflows could be set when metering airflow by varying the rotor speed.

Recommendations

It is recommended that additional simulation work be undertaken to further optimize a mis-tuned rotor design that could more accurately characterize the pressure file for extents less than 60°. It is expected that if a technique is implemented that calculated both phase and amplitude from the NSMS measurements (Figure 15), a more accurate determination of the extent would be achieved compared to the method that used amplitude only (Figure 8).

Additional simulation work should be undertaken to optimize a mistuned rotor design that could measure pressure distortion characteristics at more than three corrected airflows. To provide distortion measurements at more than three corrected speeds, it is recommended that a different frequency mis-tuning pattern be considered than the one evaluated in this thesis. The design evaluated used a ‘design point’ near the maximum rotor speed/corrected airflow that would have four different frequency blades vibrating at the same rotor speed

The other rotor speeds were more than one blade would vibrate are lower rotor speeds/corrected airflows that occur from the natural harmonics of the device. This approach resulted in too many ‘aliased’ extent occurrences where more than one extent could drive the amplitude ratios that were measured by NSMS probes. To reduce the probability that this could occur, it is recommended that an approach be undertaken to match three different blade frequencies at four rotor speed crossings with the constraint that at least one of the engine orders is an odd integer and one of the engine orders is an even integer.

Table 19 provides an example altered mis-tuning frequency pattern that provides some of the suggested frequency matching characteristics at the different rotor speeds. Additional improvement could be realized by taking advantage of the multiple occurring modes for the different blades. All of the vibratory modes model considered the fundamental 1st Bend mode only. The other modes of the blades (1st Torsion, 2nd Bend) could be designed to provide different resonant frequencies at integral EO rotor speed crossings and reduce uncertainty of the calculated extent and intensity.

LIST OF REFERENCES

1. Carter, M.B., Schuh, M., Sexton, M.R., et al, “Experimental Evaluation of Inlet Distortion on an Ejector Powered Hybrid Wing Body at Take-off and Landing Conditions”, AIAA 2016.
2. Smithsonian National Air and Space Museum, “The Wright Brothers: Invention of the Aerial Age”, Available: https://airandspace.si.edu/exhibitions/wrightbrothers/online/fly/1901/wind.cfm, Accessed April 2018.
3. Pope, Alan and Goin, Kenneth L, High Speed Wind Tunnel Testing, John Wiley & Sons, 1965.
4. Simms, D., Schreck, S., Hand, M., and Fingersh, L.J., “NREL Unsteady Aerodynamics Experiments in the NASA-Ames Wind Tunnel: A Comparison of Predictions to Measurements”, NREL Technical Report, June 2001.
5. Black, R. L, "High-speed store separation - Correlation between wind-tunnel and flight-test data." Journal of Aircraft, Vol. 6, No. 1 (1969), pp. 42-45.
6. Ferri, A., The Advisory Group for Aerospace Research and Development (AGARD) Lecture Series 53: Airframe/Engine Integration, May 1972.
7. Bousques, J.M., “"Survey of Engine Integration Testing in ONERA Wind Tunnels", 41st AIAA/ASME/SAE/ASEE Joint Propulsion Conference & Exhibit, Joint Propulsion Conference, 2005,
8. Smart, M.K., “"Experimental Testing of a Hypersonic Inlet with Rectangular-to-Elliptical Shape Transition", Journal of Propulsion and Power, Vol. 17, No. 2 (2001), pp. 276-283.
9. Shea, P.R, Flamm, J.D., Long, K., “"Turbine Powered Simulator Calibration and Testing for Hybrid Wing Body Powered Airframe Integration (Invited)", 54th AIAA Aerospace Sciences Meeting, AIAA SciTech Forum, 2016.
10. Flamm, J.D, James, K.D., Bonet, J.T., “Overview Of ERA Integrate Technology Demonstration (ITD) 51A Ultra-High Bypass (UHB)Integration for Hybrid Wing Body (HWB)”, AIAA 2015.
11. Gas Turbine Engine Inlet Flow Distortion Guidelines, Society of Automotive Engineers (SAE) Aerospace Recommended Practice 1420 Rev B, 2002, Warrendale, PA.
12. Inlet Total-Pressure Distortion Considerations for Gas-Turbine Engines, SAE Aerospace Information Report 1419 Rev A, 1999, Warrendale, PA.
13. Haberman, Richard, Elementary Applied Differential Equations with Fourier Series and Boundary Value Problems, Third Edition, Prentice Hall, New Jersey, 1998.
14. Boas, Mary L, Mathematical Methods in the Physical Sciences Second Edition, John Wiley & Sons, New York, 1983.

15. MathWorks MATLAB Documentation: Fast Fourier Transform Functions: Available: https://www.mathworks.com/help/matlab/ref/fft.html, Accessed January 2018.
16. Harrison, N.D., “Evaluation of Oscillatory Signals Generated from Rotating Machinery”, Masters Thesis, University of Tennessee, 2018.
17. Kilpatrick, D.A., Carter, D.S., and O’Neil, L “Vibratory Stresses in a Multi-Stage Axial Flow Compressor”, Ministry of Aviation Aeronautical Research Council Reports and Memorandum, UK, 1961.
18. Meher-Homji, Cyrus B., “Blading Vibration and Failures in Gas Turbines Part B: Compressor And Turbine Airfoil Distress”, American Society of Mechanical Engineers, 95-GT-419, 1995.
19. Manwaring, Stephen R., Lorence, Christopher B., Wadia, A.R., Rabe, Douglas C, “Inlet Distortion Generated Forced Response of a Low Aspect Ratio Transonic Fan”, Journal of Turbomachinery, October 1997, 97-GT-376.
20. Williams, Robert C.; Diedrich, James H.; Shaw, Robert J.; “Turbofan Blade Stresses Induced by the Flow Distortion of a VTOL Inlet at High Angles of Attack”, NASA Technical Memorandum 82963, NASA Lewis Research Center, Jan. 1983.
21. Mikolajczk, Arnold, R.A., Snyder, L.E., and Startgardter, H.,. "Advances in fan and compressor blade flutter analysis and predictions", Journal of Aircraft, Vol. 12, No. 4 (1975), pp. 325-332.
22. Frank Lane. "System Mode Shapes in the Flutter of Compressor Blade Rows", Journal of the Aeronautical Sciences, Vol. 23, No. 1 (1956), pp. 54-66.
23. Srinivasan, A.V. “Flutter and Resonant Vibration Characteristics of Engine Blades”, J. Engine Gas Turbines Power 119(4) 742-775, Oct 01 1997.
24. Peng., C. and Aurifeille, V.J., “The Nature of Choke Flutter in Low and High Pressure Compressors”, 9th National Turbine Engine High Cycle Fatigue (HCF) Conference, March 2004.
25. Besem, F.M and Kielb, R.E, “Forced Response Sensitivity of a Mistuned Rotor From an Embedded Compressor Stage”, Paper No. GT2015-43032.
26. ASME Turbo Expo 2015: Turbine Technical Conference and Exposition Volume 7B: Structures and Dynamics Montreal, Quebec, Canada, June 15–19, 2015 Conference Sponsors: International Gas Turbine Institute.

27. Castanier, M. and Pierre, C. "Investigation of the combined effects of intentional and random mistuning on the forced response of bladed

disks", 34th AIAA/ASME/SAE/ASEE Joint Propulsion Conference and Exhibit, Joint Propulsion Conferences, 1998, AIAA-98-3720.

28. Sanchez-Alvarez, J, “Maximum Mistuning Amplification of the Forced Response Vibration of Turbomachinery Rotors in the Presence of Aerodynamic Damping”, Journal of Sound and Vibration, Volume 397, 9 June 2017, Pages 108-122.
29. Kata, R.V. and Kielb R.E. "Flutter of turbofan rotors with mistuned blades", AIAA Journal, Vol. 22, No. 11 (1984), pp. 1618-1625.
30. Dugundji, J. and Bundas, D.J., "Flutter and forced response of mistuned rotors using standing wave analysis", AIAA Journal, Vol. 22, No. 11 (1984), pp. 1652-1661.
31. Zielinsk, M. and Ziller, G., “Noncontact vibration measurements on compressor rotor blades”, Measurement Science and Technology, Volume 11, Number 7
32. Hayes, B.W., “Design, Implementation, and Analysis of a Time of Arrival Measurement System for Rotating Machinery”, Masters Thesis, University of Tennessee, 2012.
33. Robinson, W.W. and Washburn, R.S., “A real time non-interference stress measurement system (NSMS) for determining aero engine blade stresses.”, Proceedings of the International Instrumentation Symposium Volume, pages 793-812, 1991.
34. Apex Turbine Testing: Blade Tip Timing Signal Processing Software: Available: https://apexturbine.com/bt/ Accessed April 2018.
35. Gavin, Henri P., “The Levenberg-Marquardt method for nonlinear least squares curve-fitting problems”, Department of Civil and Environmental Engineering Duke University March 22, 2017.
36. Arnold, S.A., Hartman, J.A, Cox, J.R., Anusonti-Inthra, P, “Development of a Turbine Engine and Compressor Test Rigs for Graduate Level Education and Research”, 51st Joint Propulsion Conference, AIAA 2015-3183.
37. Hartman, Joshua A., "Design and Fabrication of a Low-Cost Turbine Engine Component Testbed (TECT). " Master's Thesis, University of Tennessee, 2014.
38. Cox, Jon R., “Turbine Engine Rotor Blade Damage Detection through the Analysis of Vibration of Stationary Components” PhD Dissertation, University of Tennessee, 2016.
39. Overall, B., “A Procedure for the Design of Complex Distortion Screen Patterns for Producing Specified Steady-State Total Pressure Profiles at the Inlet of Turbine Engines,” Technical Report, Arnold Engineering Development Center, 1972.
40. Anderson, R., “Aircraft Engine Inlet Pressure Distortion Testing in a Ground Test Facility,” AIAA/SAE/ASME 19th Joint Propulsion Conference.

41. Ramamurthy, S., Murugesa, K., and S. Sankaranarayanan, D. R., “Design and Development of Distortion Screens for a Gas Turbine Engine Intake,” Tech. rep., National Aerospace Laboratories, Propulsion Division, 1997.
42. Anthony M. Ferrar, William C. Schneck, III, Justin M. Bailey, Kevin M. Hoopes, and Walter F. O’Brien†, “Application of Additive Manufacturing to Rapidly Produce High-Resolution Total Pressure Distortion Screens”, 50th AIAA Aerospace Sciences Meeting including the New Horizons Forum and Aerospace Exposition 09 - 12 January 2012, Nashville, Tennessee, AIAA-2012-0929.
43. Freund, O, “Non-contact test set-up for aeroelasticity in a rotating turbomachine combining a novel acoustic excitation system with tip-timing” Measurement Science Technology, Vol. 25, 2014.
44. Mathworks Simulink Documentation: Simulink Product Description, Available: https://www.mathworks.com/help/simulink/gs/product-description.html, Accessed December 2017.
45. “SIMULINK Modeling of a spring-mass-damper system”, Available https://www.youtube.com/watch?v=_DTdgp-oIUI , 1994. Accessed December 2017.

APPENDIX

Figure 1 – Wind Tunnel Test of NASA Hybrid Wind Body (HWB) Model[1].

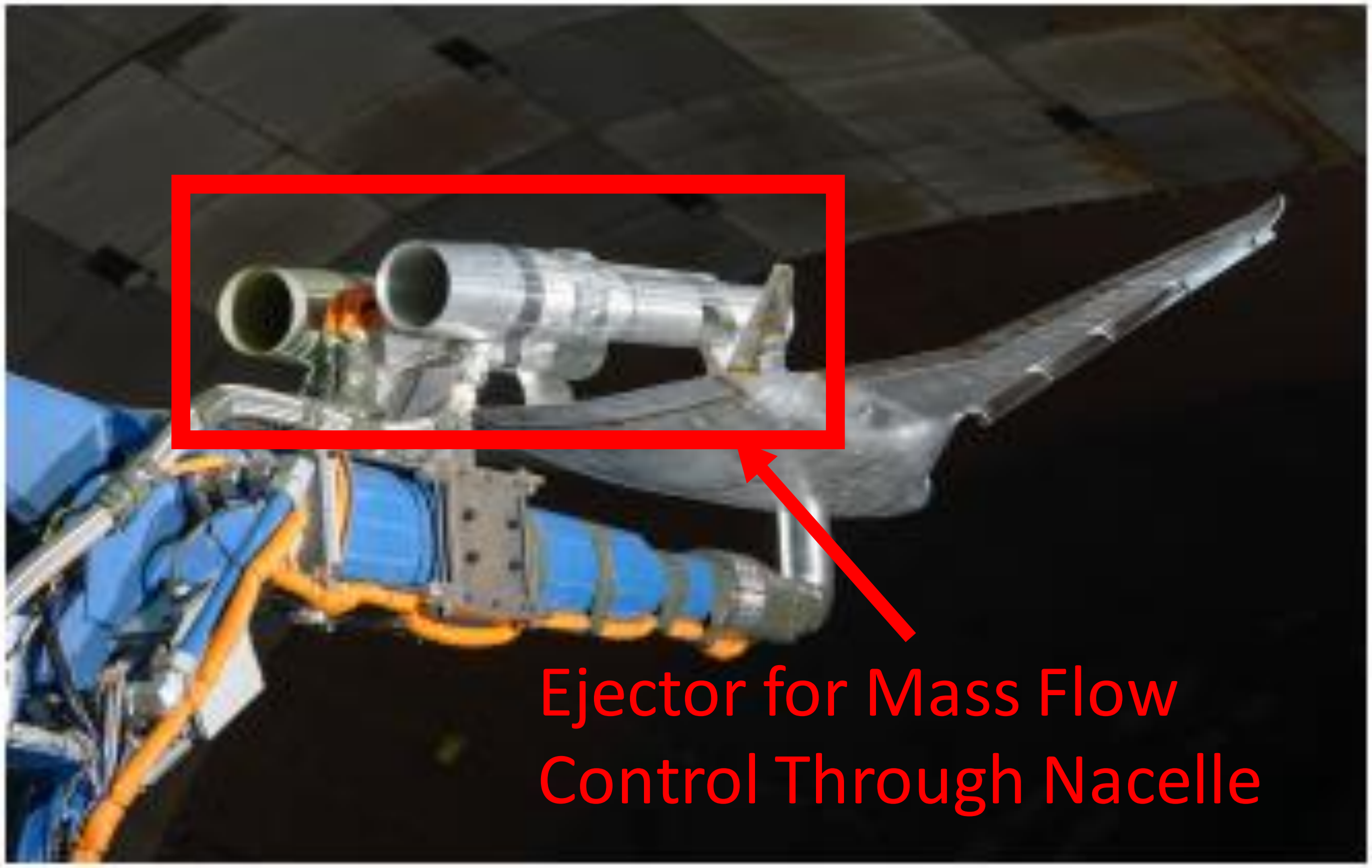

Figure 2 – HWB Model with Ejectors for Nacelle Mass Flow Control[1].

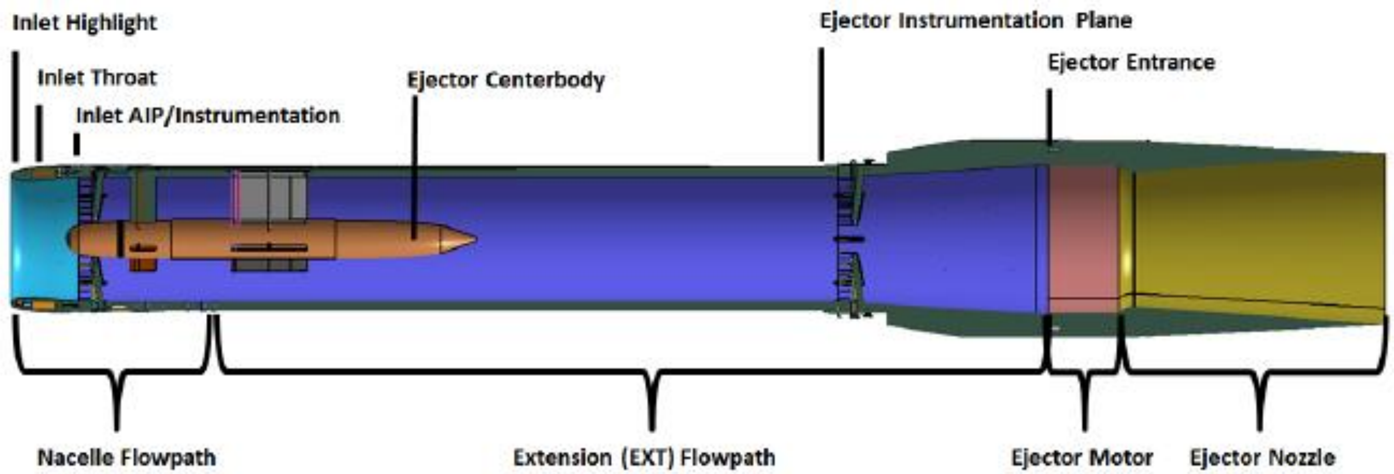

Figure 3 – Center Cut of HWB Nacelle and Ejector[1].

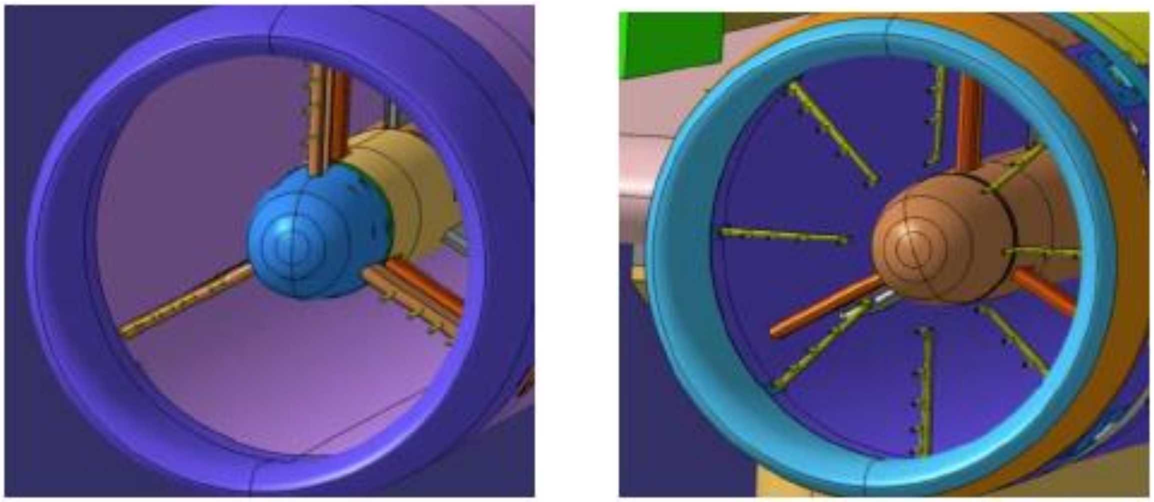

(a) Swirl rake (right inlet) (b) 40 probe rake (left inlet)

Figure 4 – HWB Model Inlet Instrumentation Configuration[1].

Table 1 – Comparison of Legacy and Proposed Technique.

	Legacy Technique	Proposed Tech. Goals
# of Measurements	40	4
Pressure Uncertainty	1 %	5 %
Spatial Resolution	2°	10°
Aeromechanical Uncert.	>10 %	<10 %
Airflow Levels	Unlimited	4
Size	Length>4xDiameter	Length=Diameter
Cost	>$5000	<$1000

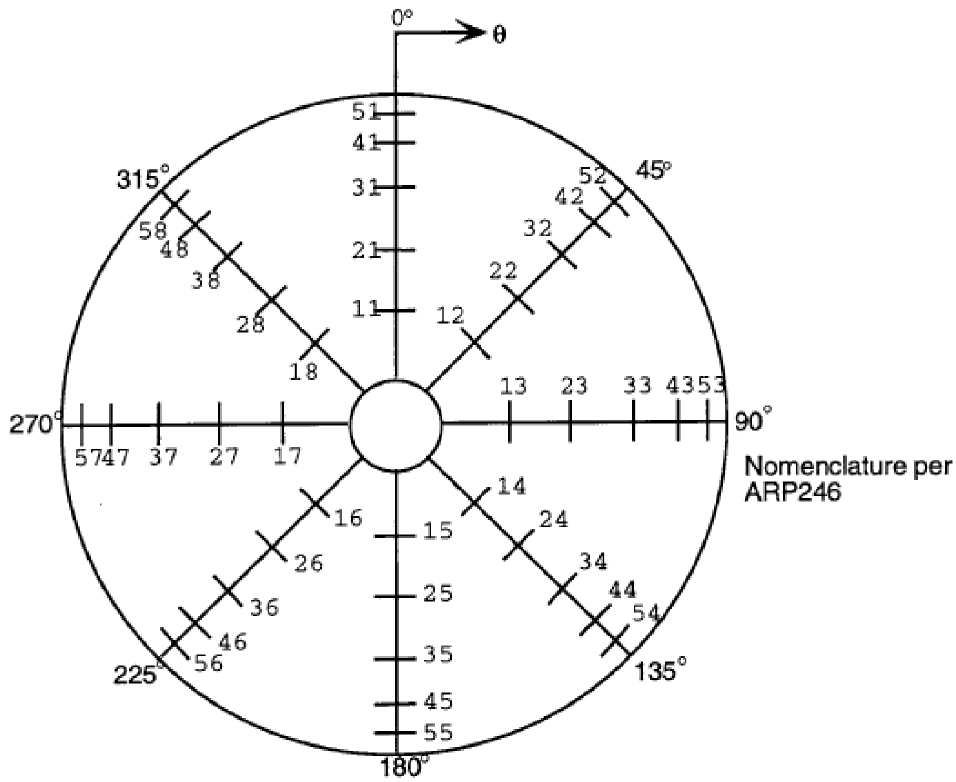

Figure 5 – Circumferential - ARP 1420 Recommended Total Pressure Measurements[8].

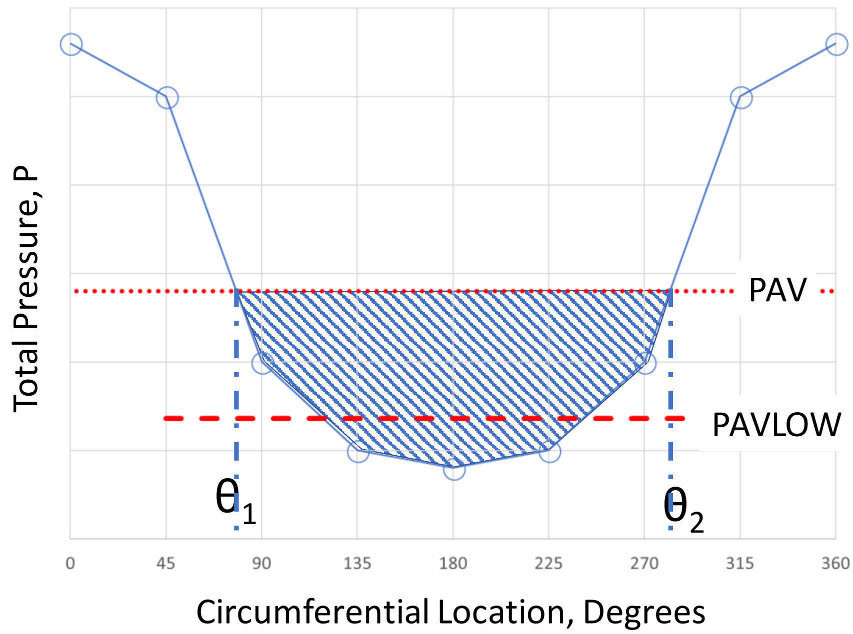

Figure 6 – Circumferential Pressure Measurements for Distortion Descriptors.

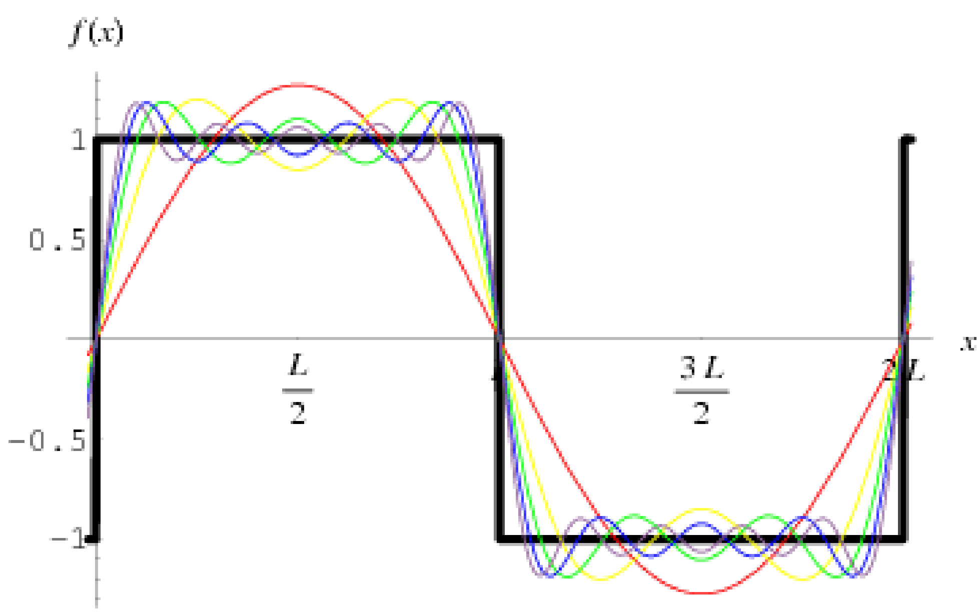

Figure 7 – Fourier Series of Odd Harmonics of Sine Function.

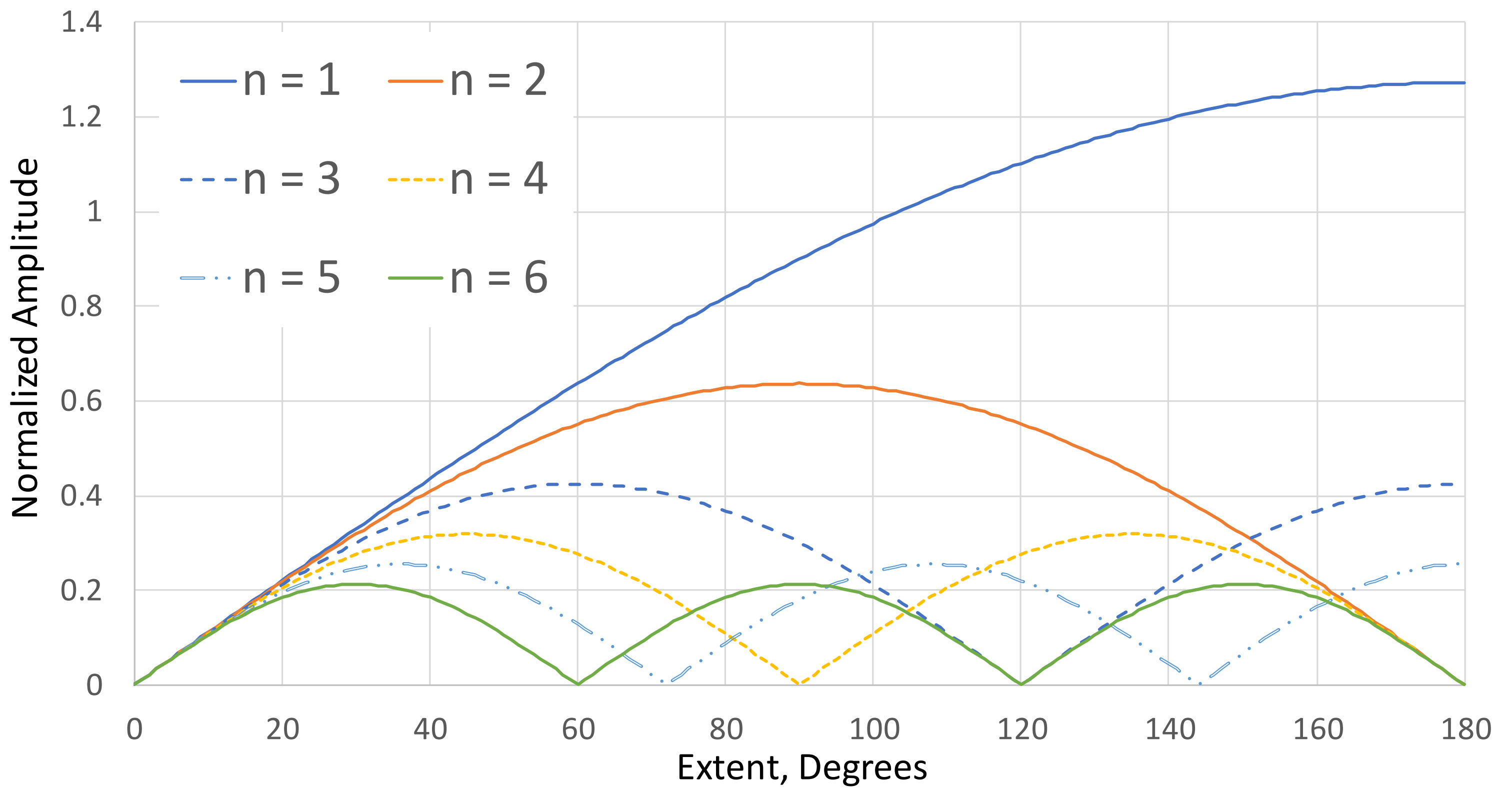

Figure 8 – Fourier Series Coefficient for Different Extent & n.

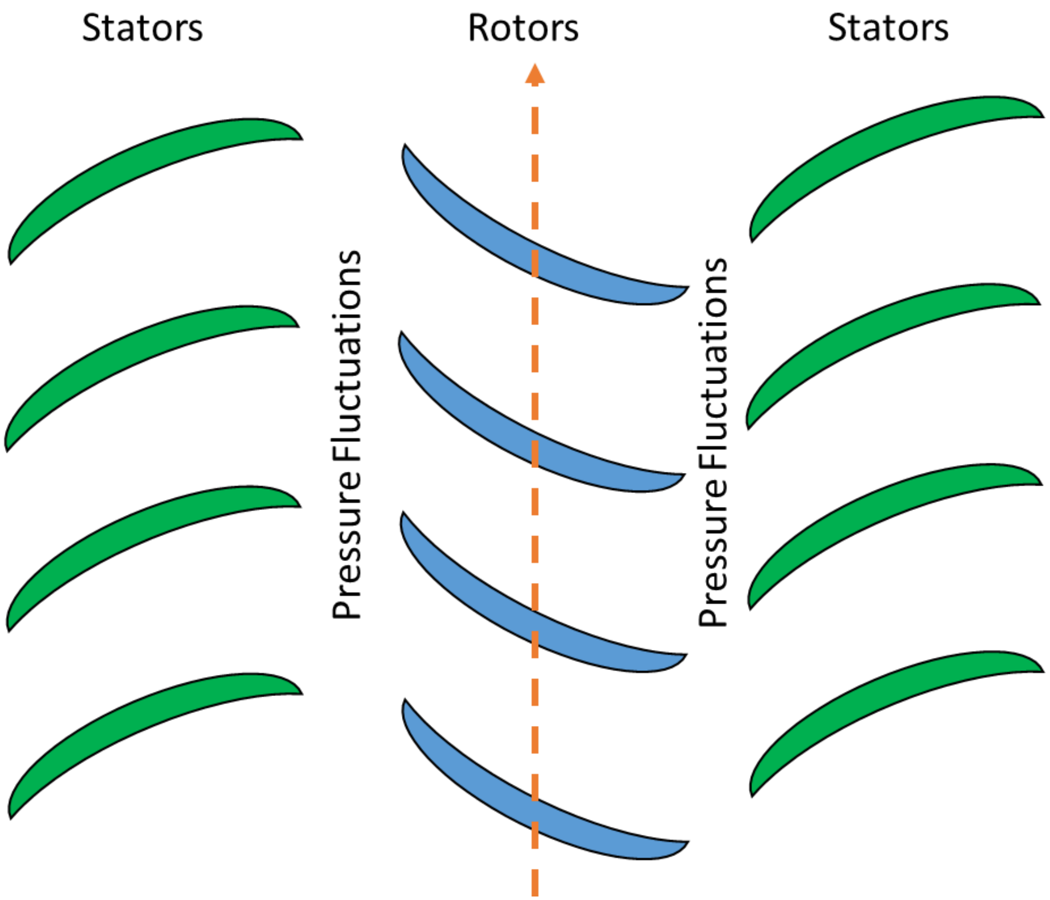

Figure 9 – Example Rotating Blade Row Passing By Stationary[16]

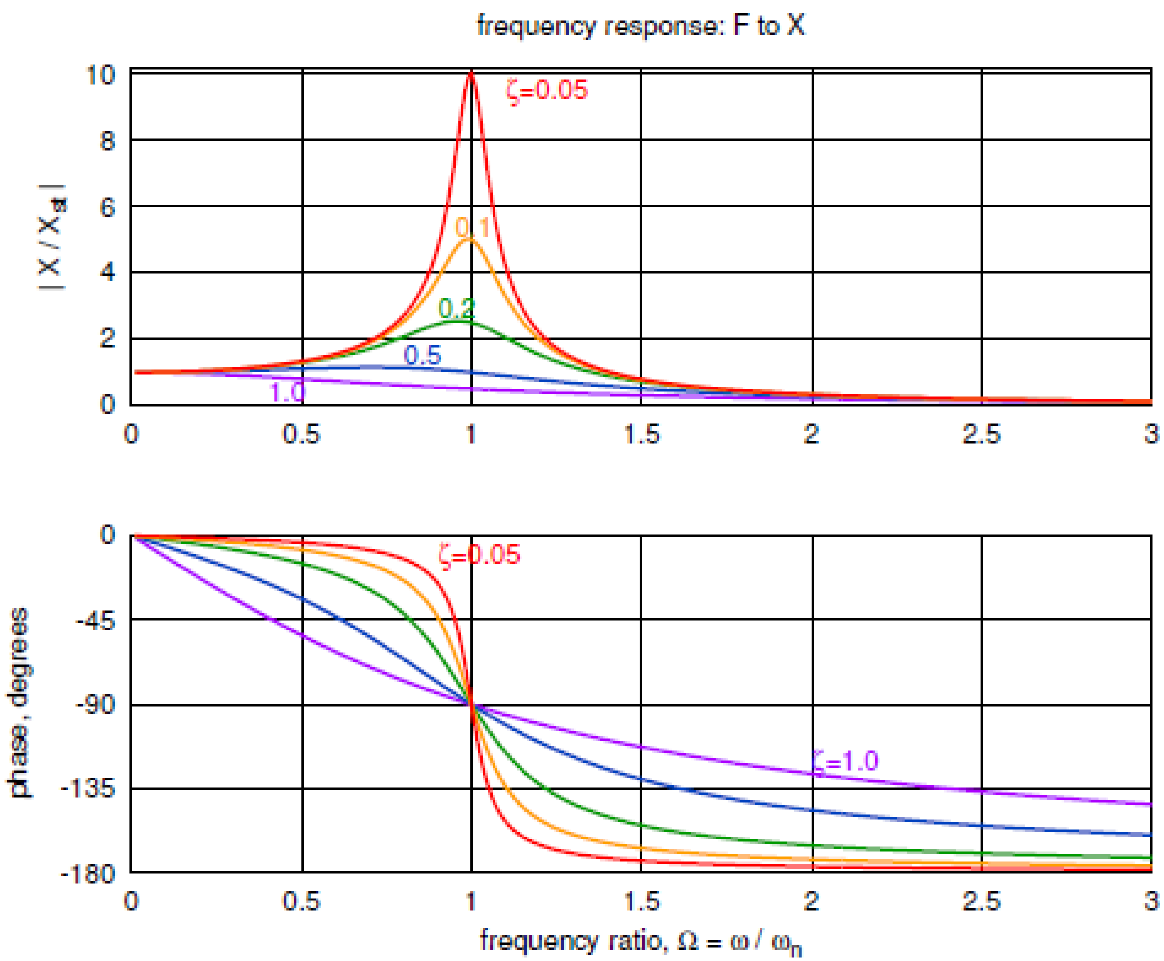

Figure 10 – Amplification Factor and Phase Change With Varying Excitation Frequency.

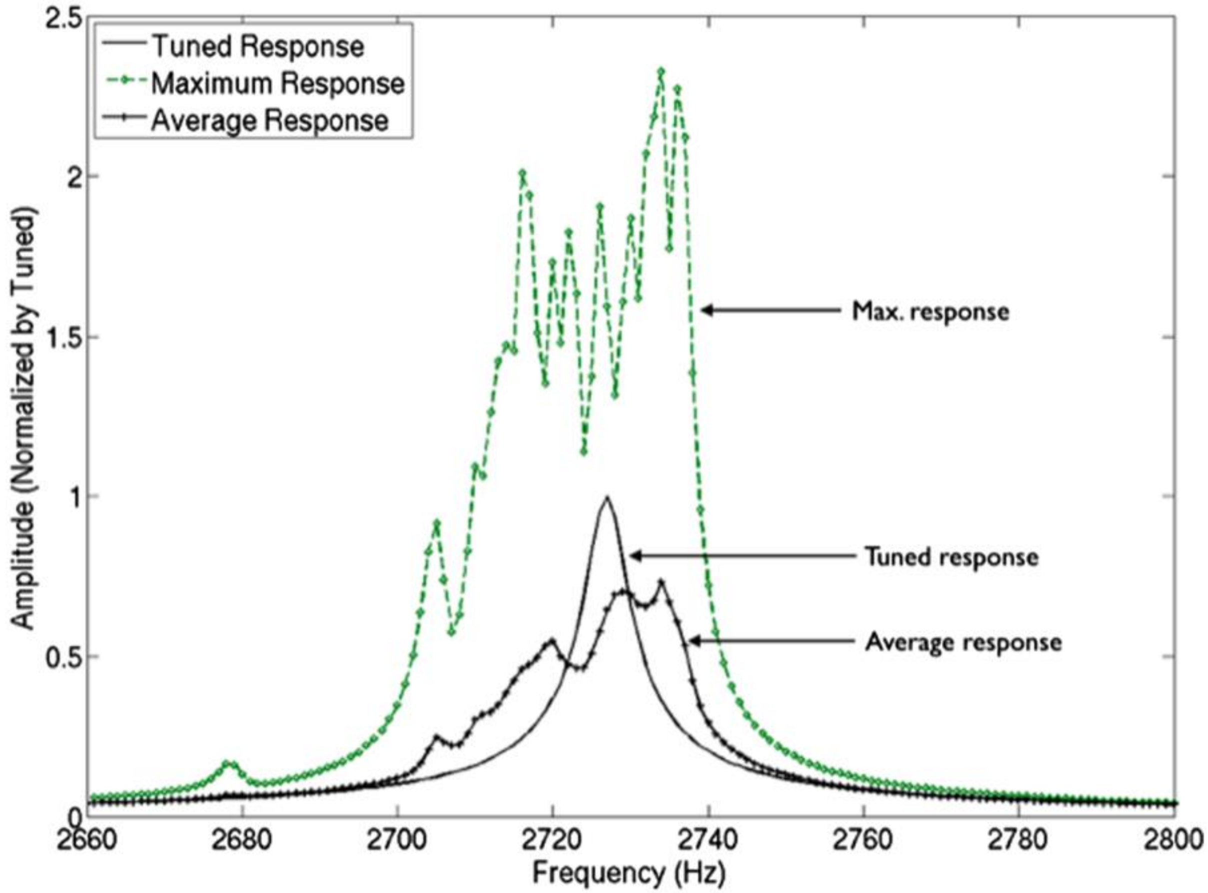

Figure 11 – Example Forced Response Amplitude Increase for Mis-Tuned Rotor[27].

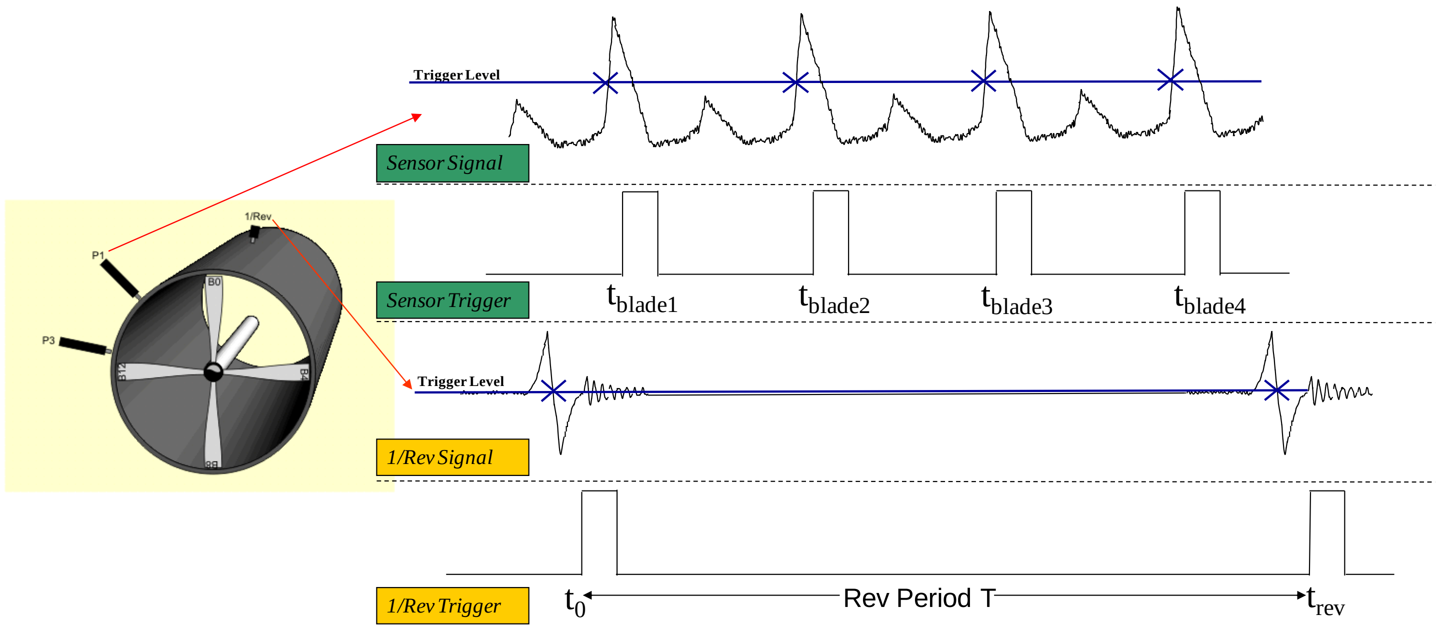

Figure 12 – Example Time of Arrival Measurement for 4 Blade Rotor[32].

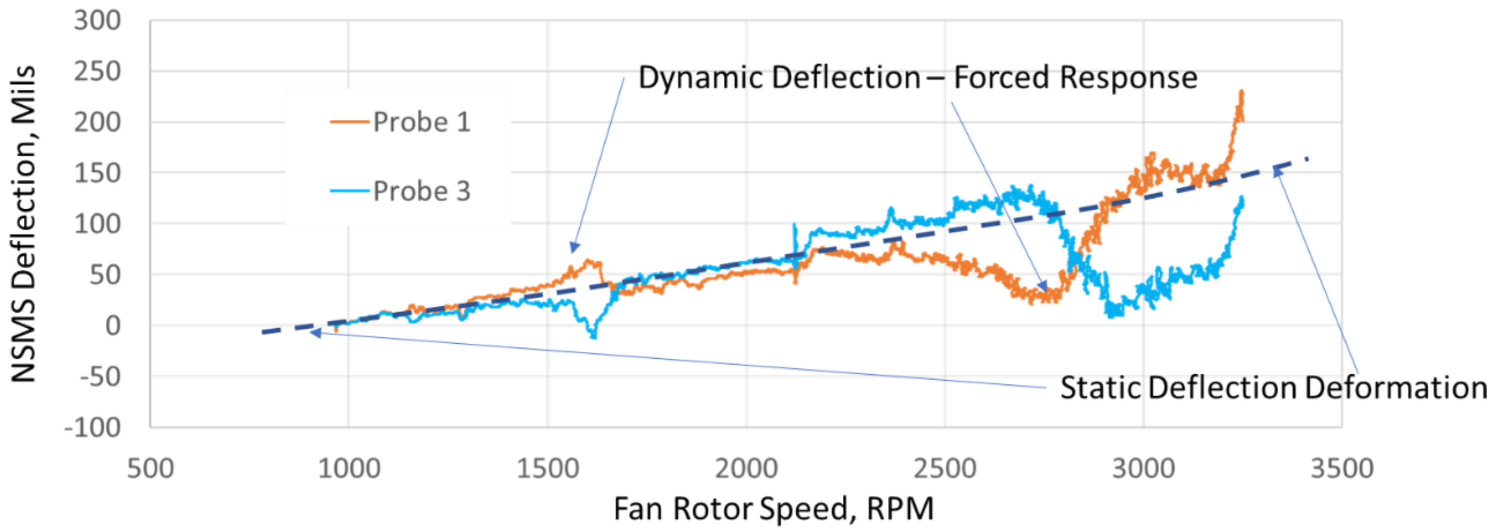

Figure 13 –NSMS Measurements with Static and Dynamic Deflection.

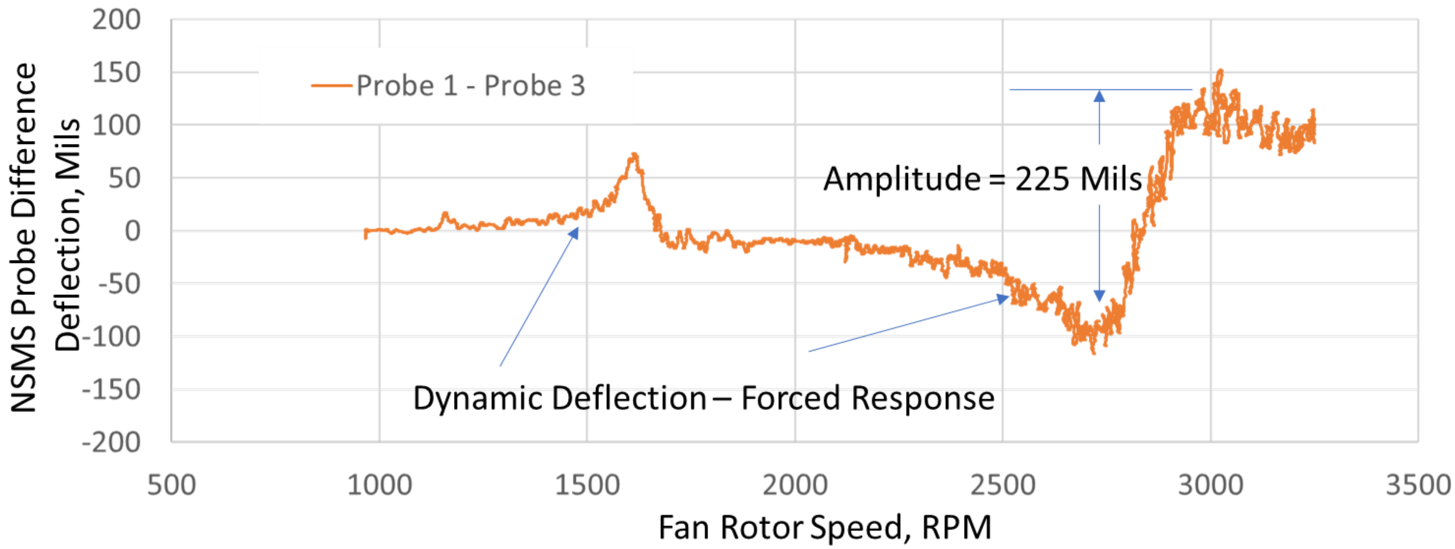

Figure 14 – Example Probe Difference NSMS Measurement from Fan Rig.

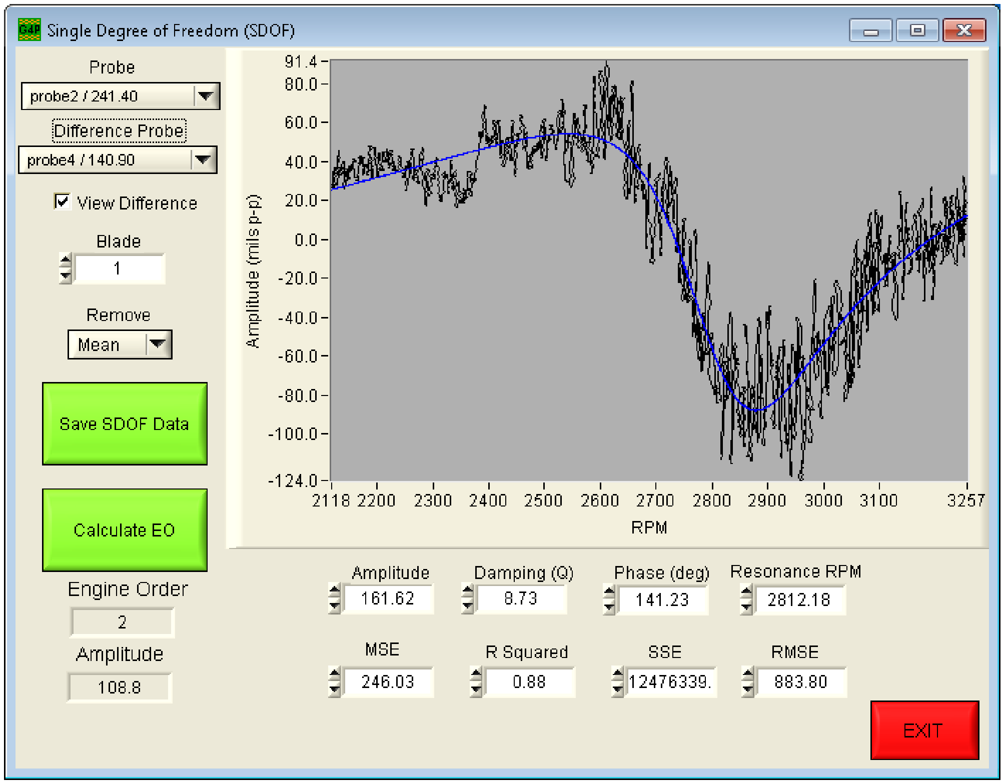

Figure 15 – NSMS Amplitude, Damping, Frequency, and Phase from Lavenburg-Marquedt Non-Linear Least Squares Solution[34].

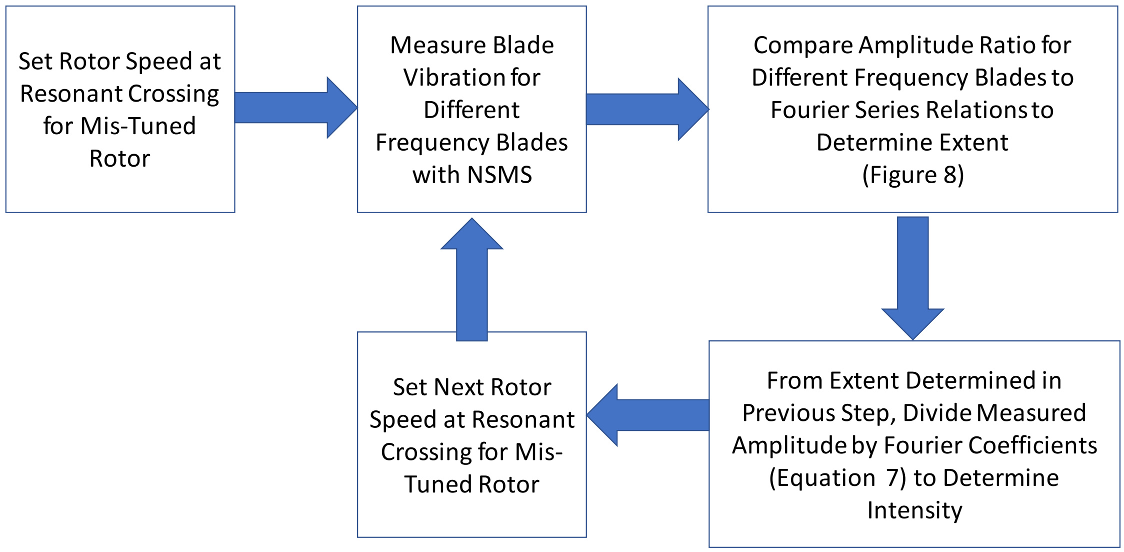

Figure 16 – Steps from Measuring Mis-Tuned Rotor Blade Vibration to Determine Pressure Distortion Extent and Intensity.

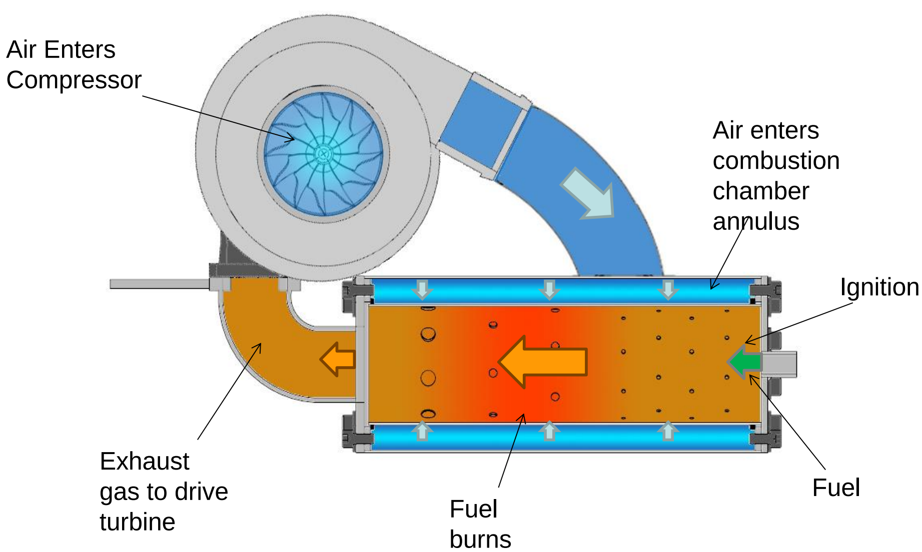

Figure 17 – Compressor and Combustor Arrangement for J1-H-01.

Figure 18 – GTE J1-H-01 Operating in Full Augmentation.

Figure 19 – Experimental Fan Rig with 3-D Printed Components.

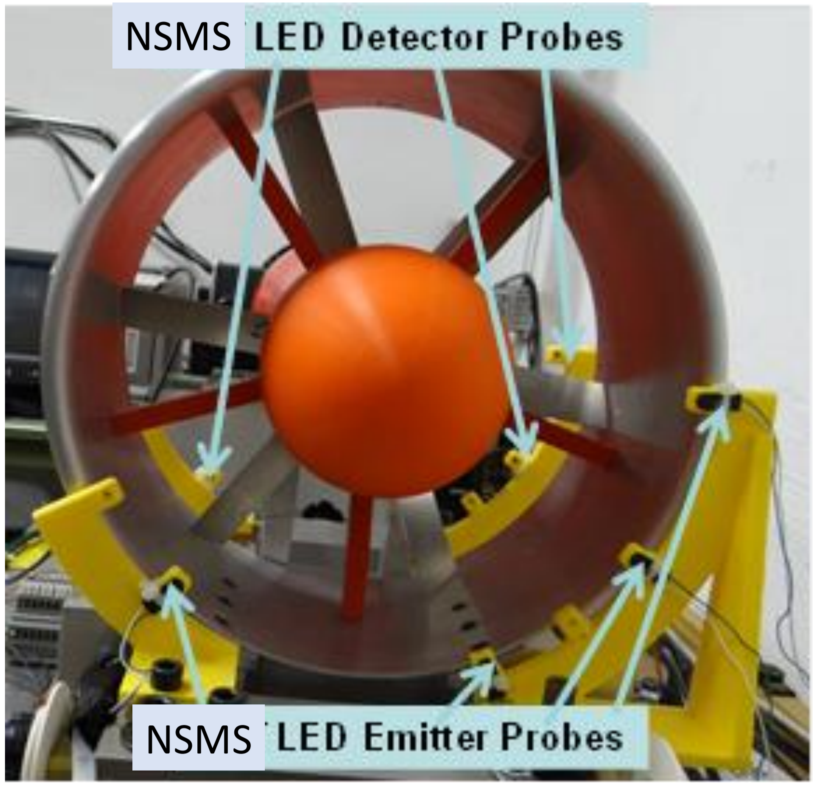

Figure 20 – NSMS Beam Interrupt Probe Mounting for Fan Rig.

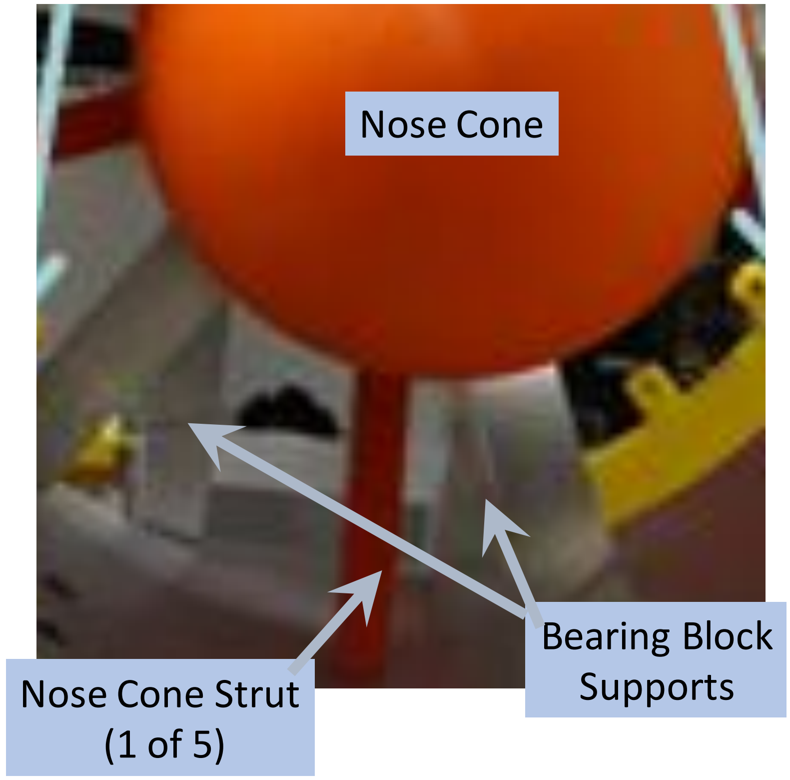

Figure 21 –View of Nose Cone Struts and Bearing Block Support.

Figure 22 – 90° Inlet Distortion Sector Installed in Fan Rig.

Table 2 – Critical Test Rig Dimensions and Properties.

Component	Length Inches	Width inches	Thickness Inches	1st Bend Frequency Hz
Rotor Hub	4.3”	N/A	1.0”	
Fan Casing	12.0”	N/A	0.075”	
Thin Blade	3.8”	1.4”	0.031”	63 Hz
Nominal Blade	3.8”	1.4”	0.062”	83 Hz
Thick Blade	3.8”	1.4”	0.125”	125 Hz

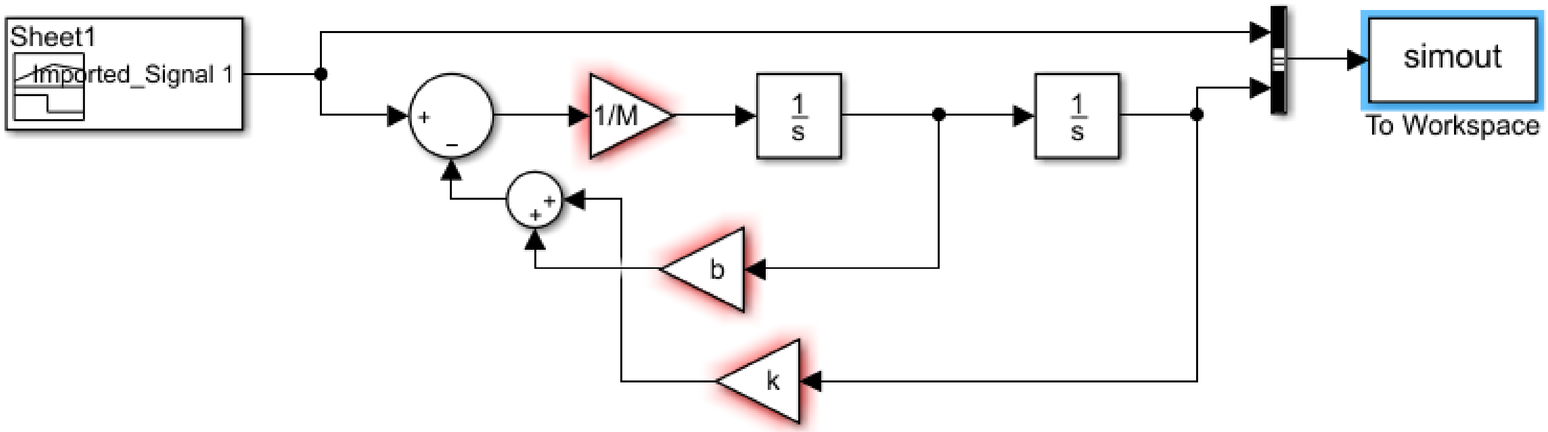

Figure 23 - Simulink® Block Diagram of SDOF Modeling of Fan Rig Blade.

Table 3 – Original Experiment Test Matrix

Case #	Extent	Intensity	Clocking
1	None	None	None
2	90°	Honeycomb	Top Dead Center
3	90°	Honeycomb + Mesh	Top Dead Center
4	90°	Honeycomb	72 Degree
5	135°	Honeycomb	Top Dead Center
6	45°	Honeycomb	Top Dead Center

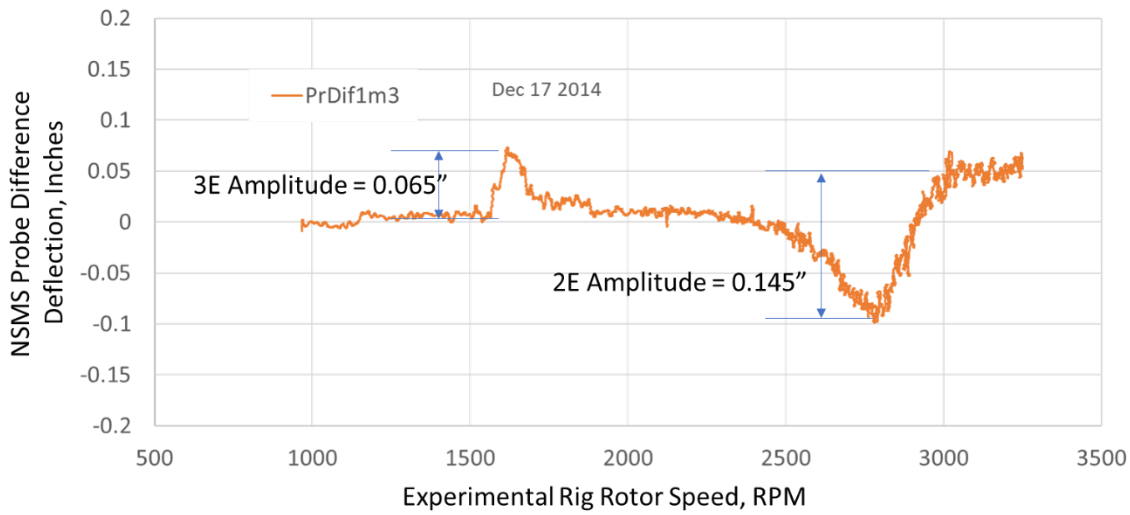

Figure 24 – Example NSMS Measurement without Distortion Blockage

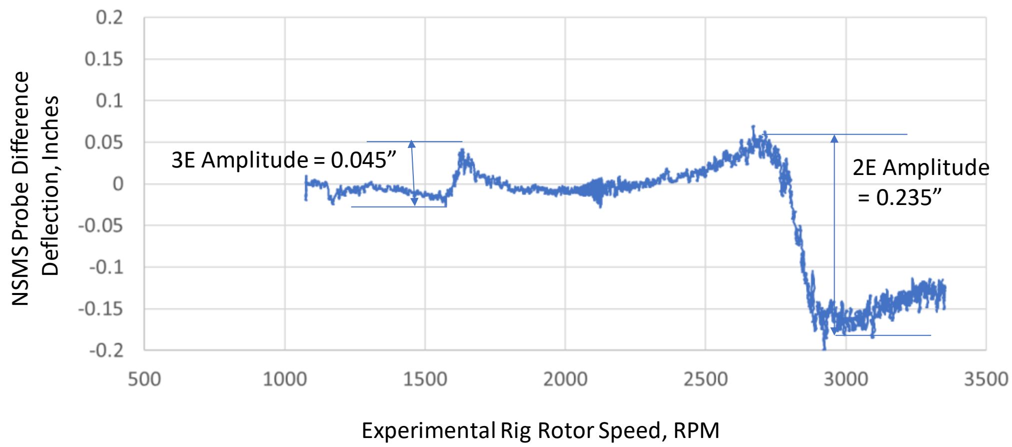

Figure 25 – NSMS Measurements with 90° Extent Distortion Blockage.

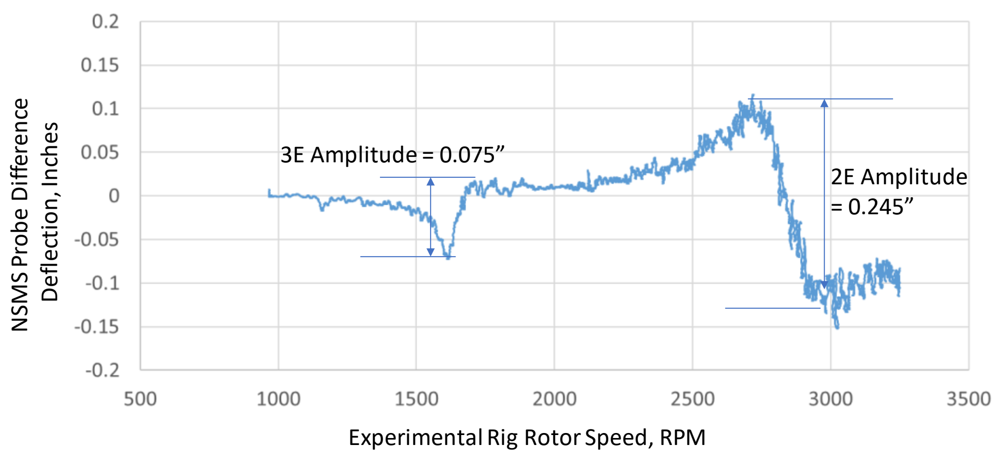

Figure 26 – Blade Response with Tape Between Bearing Block Supports.

Table 4 – Average 2E Response Characteristics for Different Configurations

Date	90° Blockage	Blockage Angle	Mesh	Bearing Block Tape	Struts	Amp Mils P-P	Freq Hz	C/C_{crit}
10/29/14	No	N/A	No	No	No	107.7	93.6	0.046
12/3/14	Yes	72°	Yes	No	Yes	107.8	95.8	0.048
10/22/14	No	N/A	No	No	Yes	140.8	94.4	0.049
11/19/14	Yes	0°	No	No	Yes	197.8	93.7	0.045
11/26/14	Yes	0°	Yes	No	Yes	229.4	94.6	0.047
12/17/14	No	N/A	No	Yes	Yes	239.3	94.0	0.047

Table 5 – Average 3E Response Characteristics for Different Configurations

Date	90° Blockage	Blockage Angle	Mesh	Bearing Block Tape	Struts	Amp Mils P-P	Freq Hz	C/C_{crit}
11/19/14	Yes	N/A	No	No	Yes	22.7	80.7	0.015
11/26/14	Yes	0°	Yes	No	Yes	26.9	80.8	0.016
10/29/14	No	N/A	No	No	No	41.1	80.3	0.028
12/17/14	No	N/A	No	No	Yes	45.9	8.15	0.019
12/3/14	Yes	72°	Yes	No	Yes	66.9	81.0	0.028
12/17/14	No	N/A	No	Yes	Yes	71.6	81.3	0.026

Table 6 – Average 4E Response Characteristics for Different Configurations

Date	90° Blockage	Blockage Angle	Mesh	Bearing Block Tape	Struts	Amp Mils P-P	Freq Hz	C/C_{crit}
12/17/14	No	N/A	No	No	Yes	13.5	78.0	0.011
12/17/14	No	N/A	No	Yes	Yes	18.1	78.4	0.020
11/19/14	Yes	0°	No	No	Yes	20.4	75.4	0.021
11/26/14	Yes	0°	Yes	No	Yes	32.9	77.9	0.017
12/3/14	Yes	72°	Yes	No	Yes	42.3	77.7	0.015

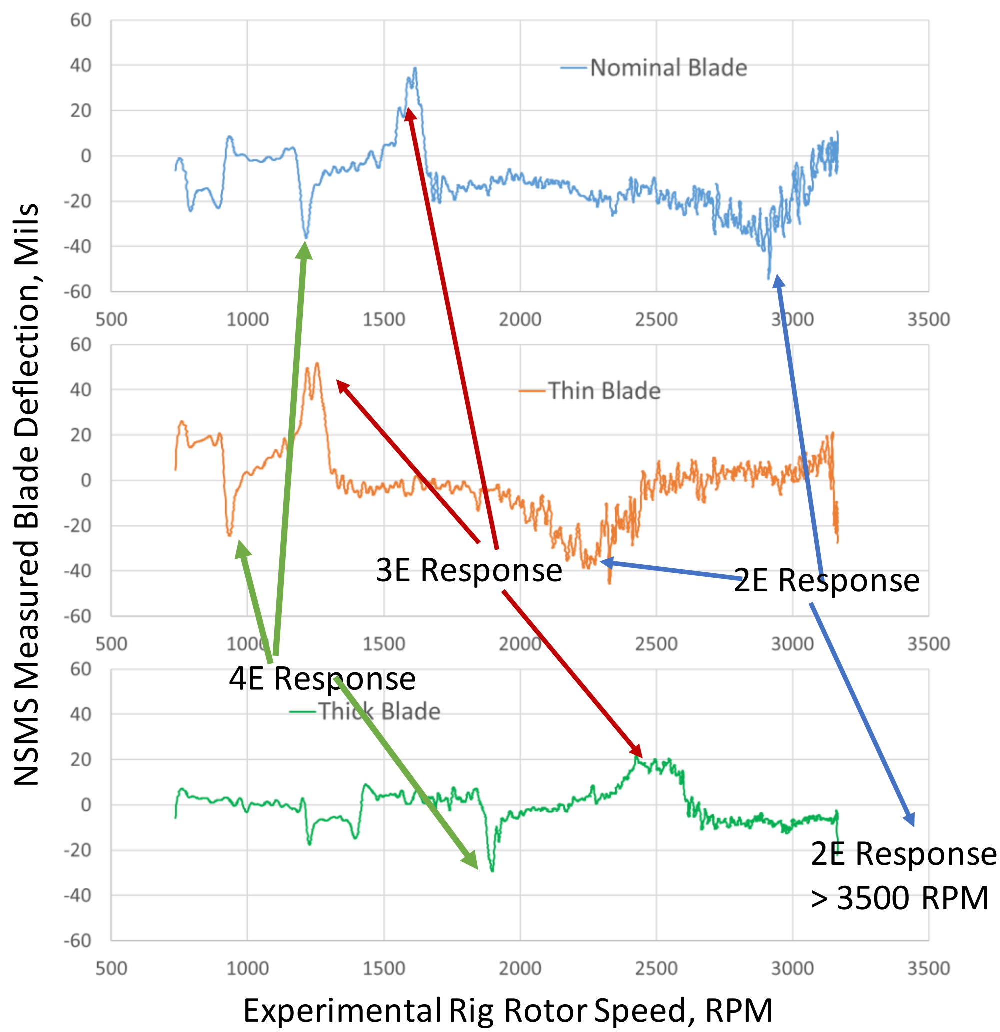

Figure 27 – Measured Responses Mis-Tuned Rotor.

Table 7 – Resonant Frequencies for Mis-Tuned Rotor.

Blade Type	2E Speed	2E Freq	3E Speed	3E Freq	4E Speed	4E Freq
	RPM	Hz	RPM	Hz	RPM	Hz
Nominal	2895	96.5	1619	80.9	1215	81
Thin	2230	74.3	1257	62.9	932	62.1
Thick	NA	NA	2550	127.5	1900	126.7

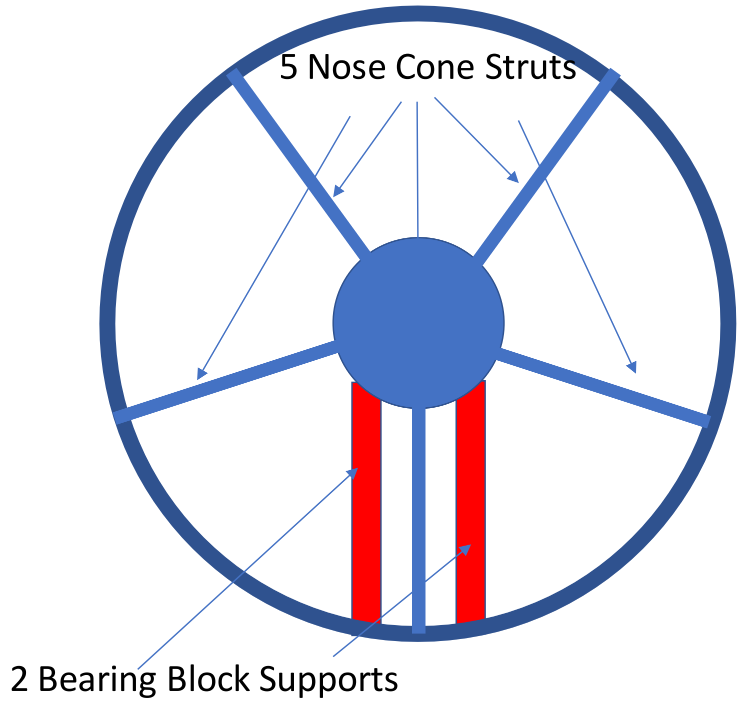

Figure 28 – Angular Location of Test Rig Struts and Supports.

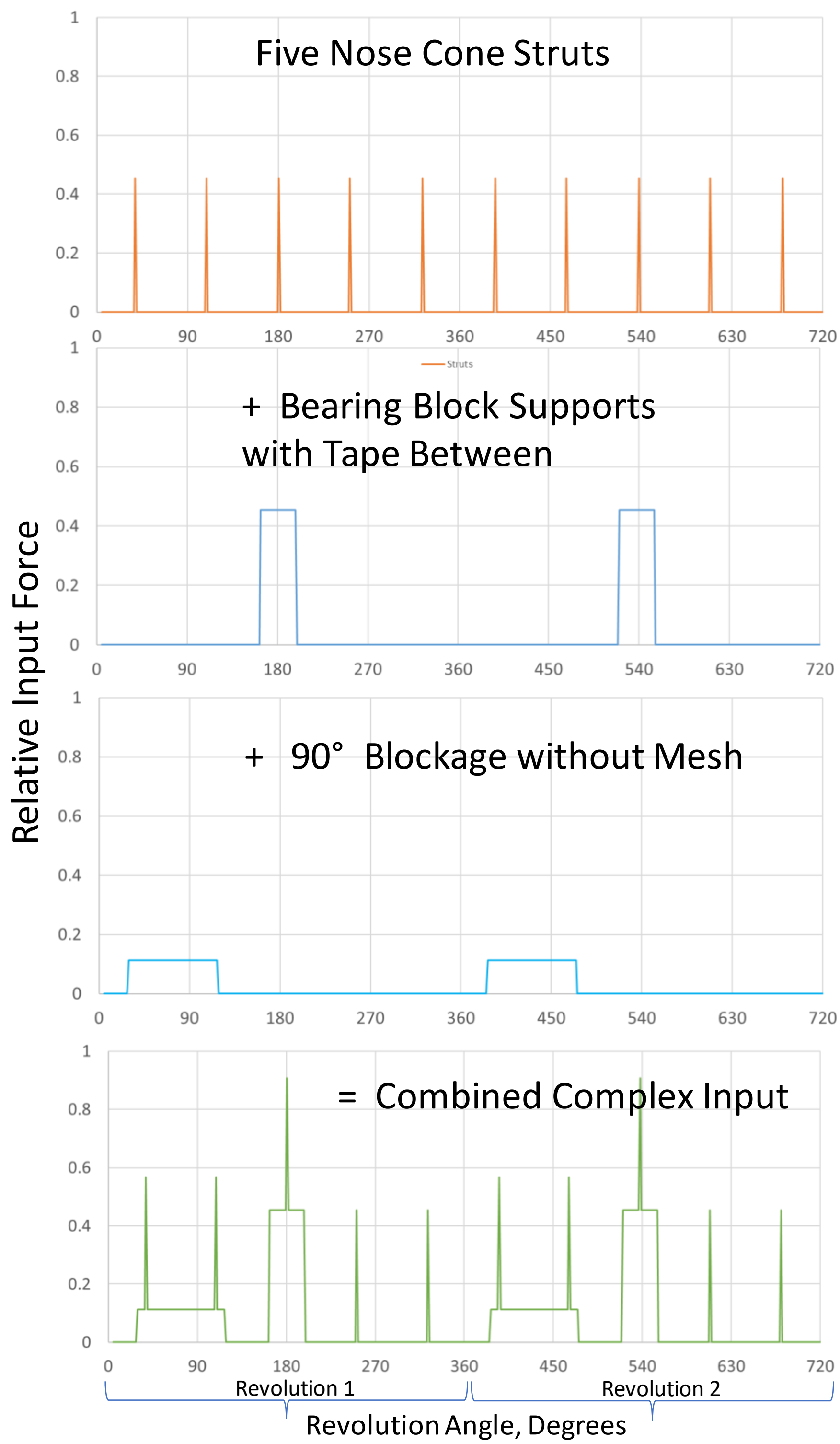

Figure 29 – Example Addition of Elements for Complex Input.

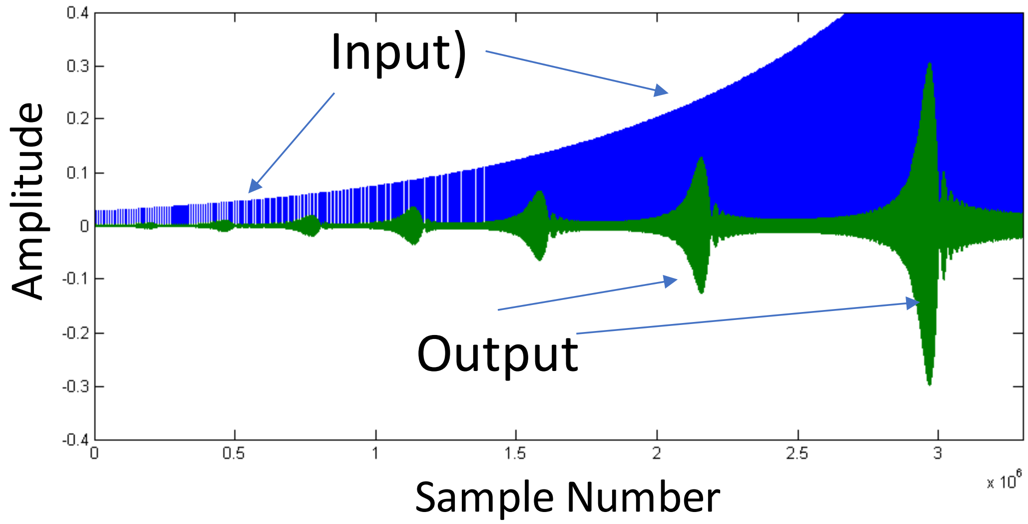

Figure 30 – Example Input Amplitude Increase During Rotor Acceleration.

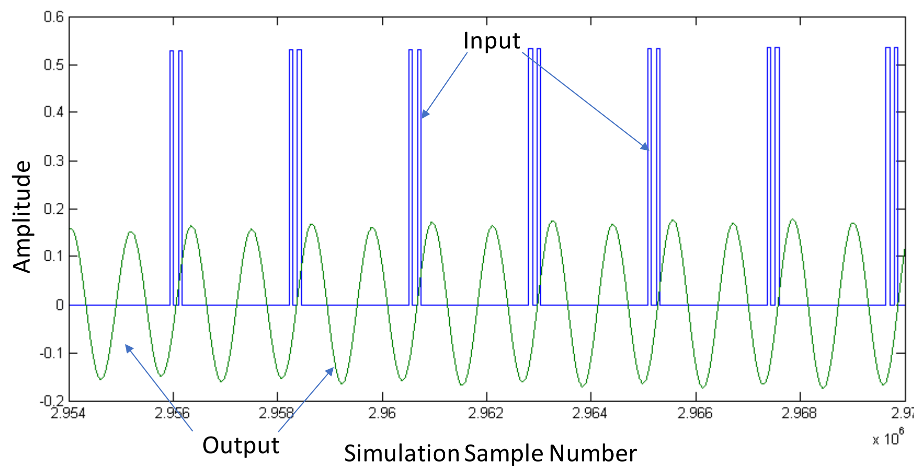

Figure 31 – Simulation Output for Bearing Block Support Input Only.

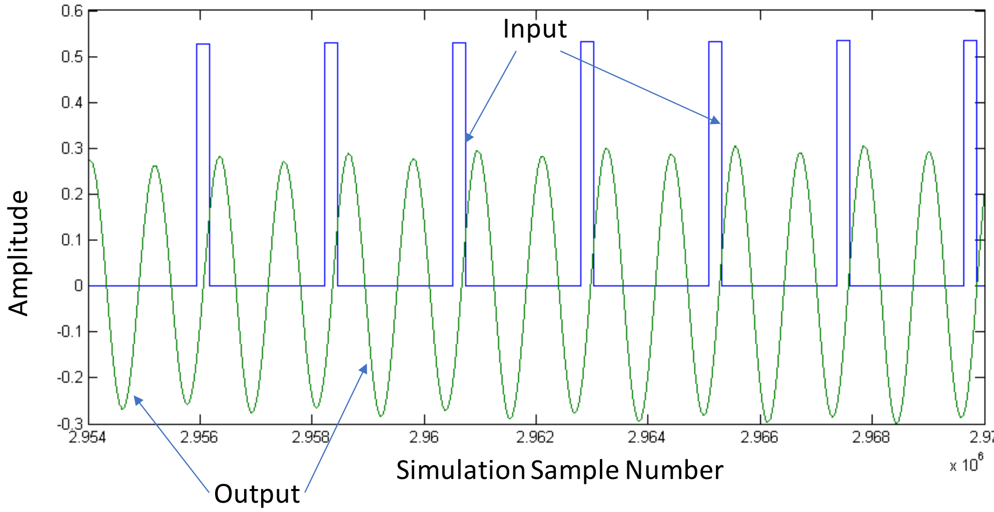

Figure 32 – Simulation Output for Bearing Block Supports with Tape Input.

Table 8 – Comparison of Experimental and Simulation 2E Amplitudes.

90° Blockage	Blockage Angle	Mesh	Bearing Block Tape	Struts	Experiment Mils P-P	Simulated Mils P-P	% Delta
No	N/A	No	No	No	107.7	90	-16%
Yes	72°	Yes	No	Yes	107.8	105.0	-2.7%
No	N/A	No	No	Yes	140.8		
Yes	0°	No	No	Yes	197.8		
Yes	0°	Yes	No	Yes	229.4	215.0	-6.3%
No	N/A	No	Yes	Yes	239.3	235.0	-1.8%

Table 9 – Comparison of Experimental and Simulation 3E Amplitudes.

90° Blockage	Blockage Angle	Mesh	Bearing Block Tape	Struts	Experiment Mils P-P	Simulated Mils P-P	% Delta
Yes	N/A	No	No	Yes	22.7		
Yes	0°	Yes	No	Yes	26.9	30.0	11.7%
No	N/A	No	No	No	41.1	35.0	-14%
No	N/A	No	No	Yes	45.9		
Yes	72°	Yes	No	Yes	66.9	80.0	19.5%
No	N/A	No	Yes	Yes	71.6	55	-23%

Table 10 – Comparison of Experimental and Simulation 4E Amplitudes.

90° Blockage	Blockage Angle	Mesh	Bearing Block Tape	Struts	Experiment Mils P-P	Simulated Mils P-P	% Delta
No	N/A	No	No	Yes	13.5		
No	N/A	No	Yes	Yes	18.1	25	37.9%
Yes	0°	No	No	Yes	20.4		
Yes	0°	Yes	No	Yes	32.9	30.0	-8.8%
Yes	72°	Yes	No	Yes	42.3		

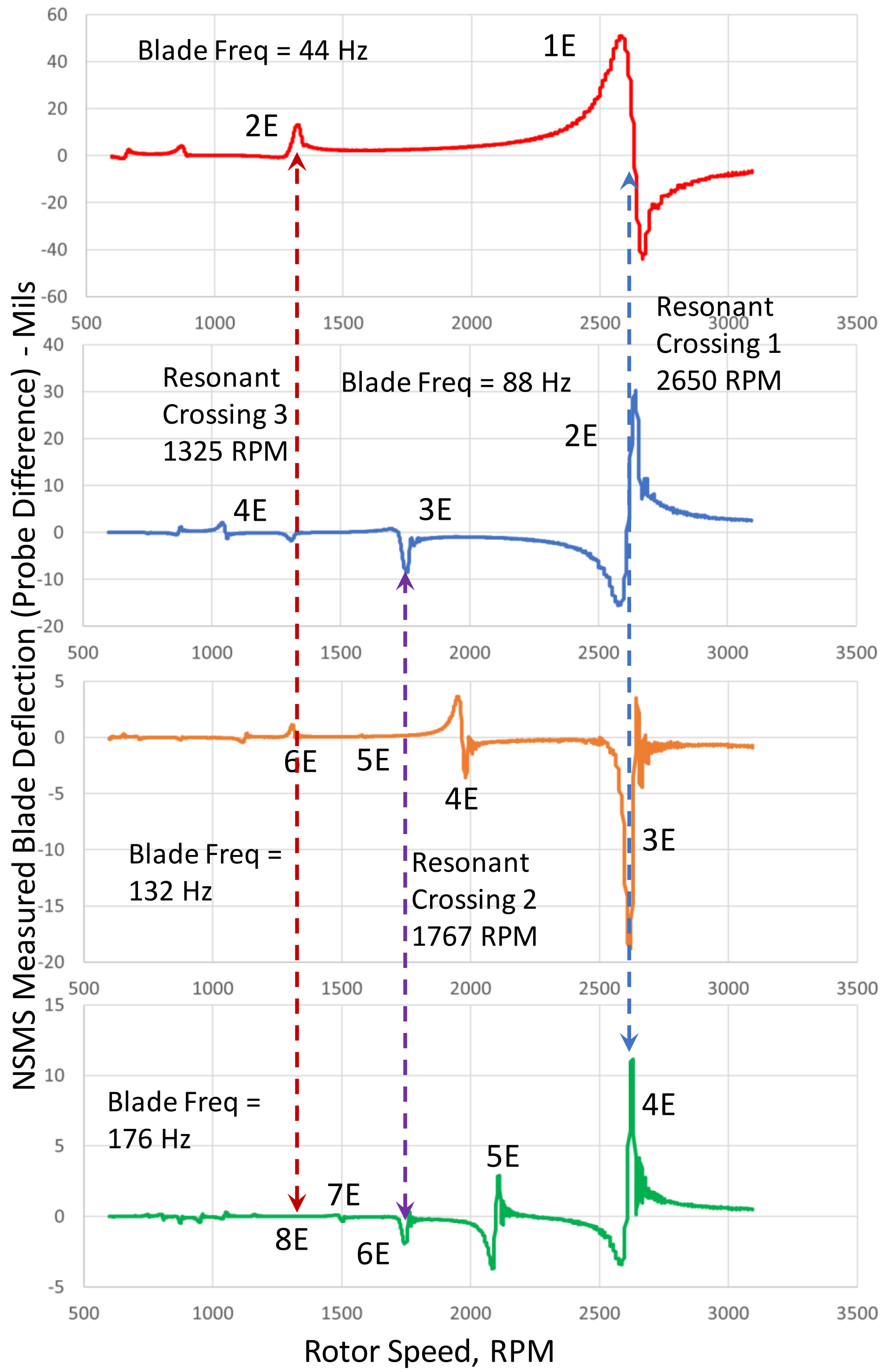

Figure 33 – Simulated Mistuned Rotor Response with 45° Extent.

Table 11 – Resonant Crossings for Simulation Analysis

Resonant Crossing #	Rotor Speed, RPM	44 Hz Blade E	88 Hz Blade E	132 Hz Blade E	176 Hz Blade E
1	2650	1E	2E	3E	4E
2	1767	NA	3E	NA	6E
3	1325	2E	4E	6E	8E

Table 12 – Extent for Different Simulation Cases

Simulation Case #	Extent
1	30°
2	45°
3	75°
4	100°
5	120°
6	135°
7	180°

Table 13 – Probe Combinations for Maximum Engine Order Deflection

Engine Order	Probe Difference	Difference Scalar
1E	274.8° - 140.9°	1.840
2E	241.4° – 140.9°	1.967
3E	205.2° – 140.9°	1.987
4E	274.8° - 140.9°	1.999
6E	274.8° - 241.4°	1.968
8E	274.8° - 205.2°	1.978

Table 14 – NSMS Simulations for 2650 RPM Resonant Crossing

Extent	1E Amp Mils P-P	2E Amp Mils P-P	3E Amp Mils P-P	4E Amp Mils P-P
30°	62.3	32.3	15.9	12.9
45°	94.7	45.7	22.3	14.6
75°	151.2	59.6	24.5	7.1
100°	190.2	56.7	13.4	5.0
120°	212.6	46.4	0.6	13.0
135°	228.5	40.4	9.1	14.7
180°	238.5	1.4	25.7	0.4

Table 15 – 2650 RPM Resonant Crossing Adjusted Amplitudes.

Extent	1E Amp Mils P-P	2E Amp Mils P-P	3E Amp Mils P-P	4E Amp Mils P-P
30°	66.7	65.8	48.1	51.8
45°	102.9	93.0	67.4	58.2
75°	164.4	121.3	74.0	28.4
100°	206.7	115.3	40.5	20.1
120°	231.1	94.4	1.8	51.8
135°	248.4	82.2	27.6	58.9
180°	259.2	2.9	77.6	1.4

Table 16 – 1767 RPM Resonant Crossing Adjusted Amplitudes

Extent	3E Amp Mils P-P	6E Amp Mils P-P
30°	23.8	18.9
45°	32.8	13.8
75°	33.7	11.3
100°	18.0	16.0
120°	0.5	1.0
135°	11.9	14.3
180°	36.4	0.6

Table 17 – 1325 RPM Resonant Crossing Adjusted Amplitudes

Extent	2E Amp Mils P-P	4E Amp Mils P-P	6E Amp Mils P-P	8E Amp Mils P-P
30°	16.7	10.4	7.5	6.7
45°	23.7	13.0	5.1	4.4
75°	31.2	22.3	5.6	6.7
100°	30.7	3.9	5.9	4.3
120°	24.2	10.4	0.6	6.6
135°	19.3	13.0	5.7	0.0
180°	0.8	0.5	0.3	0.6

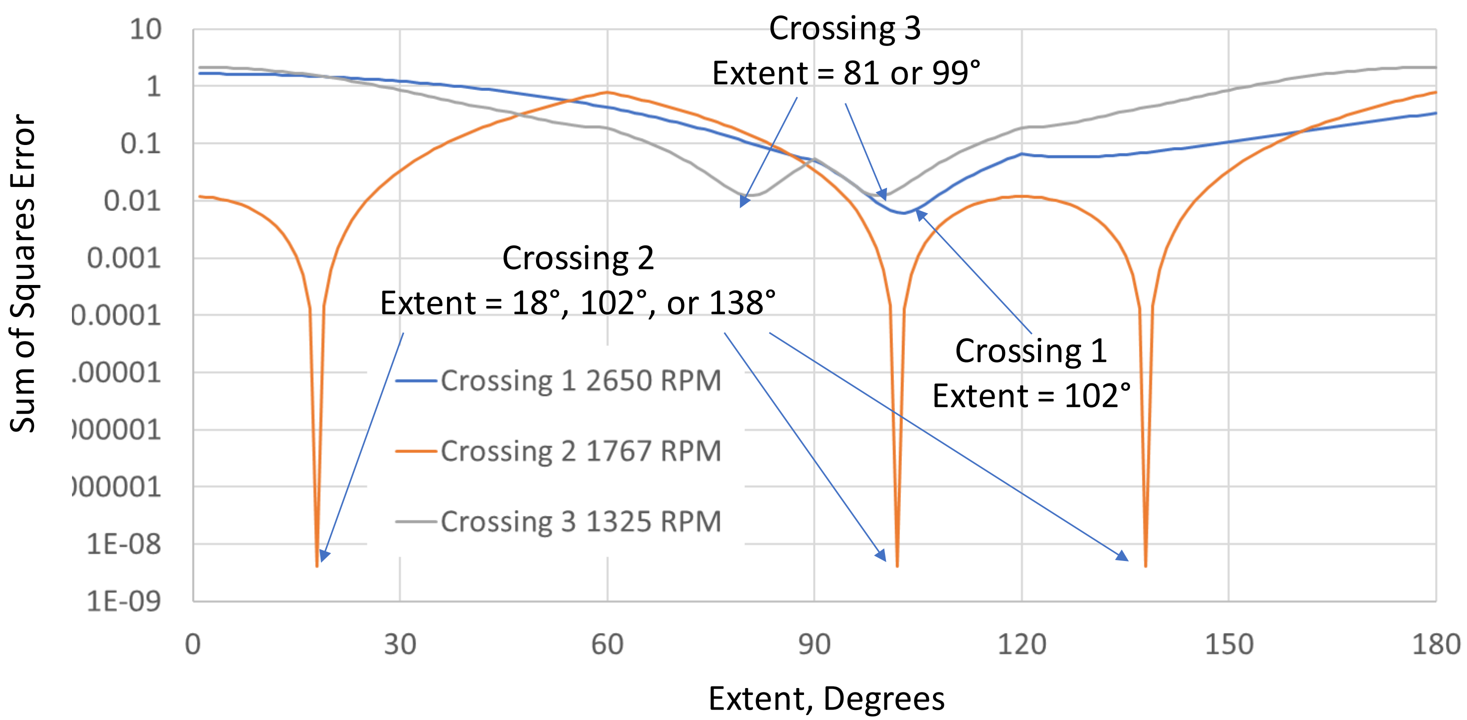

Figure 34 – Example Sum of Square Error for 100° Extent.

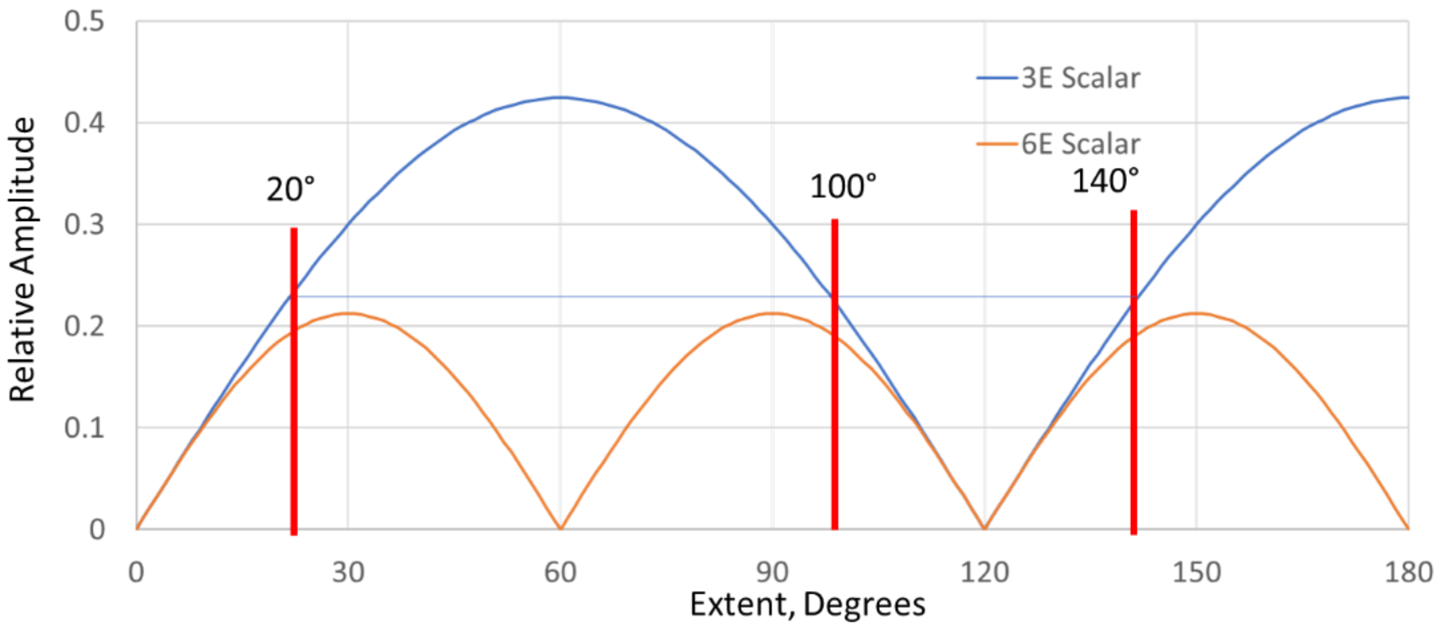

Figure 35 – Example 3E & 6E Amplitudes at 20°, 100°, and 140°.

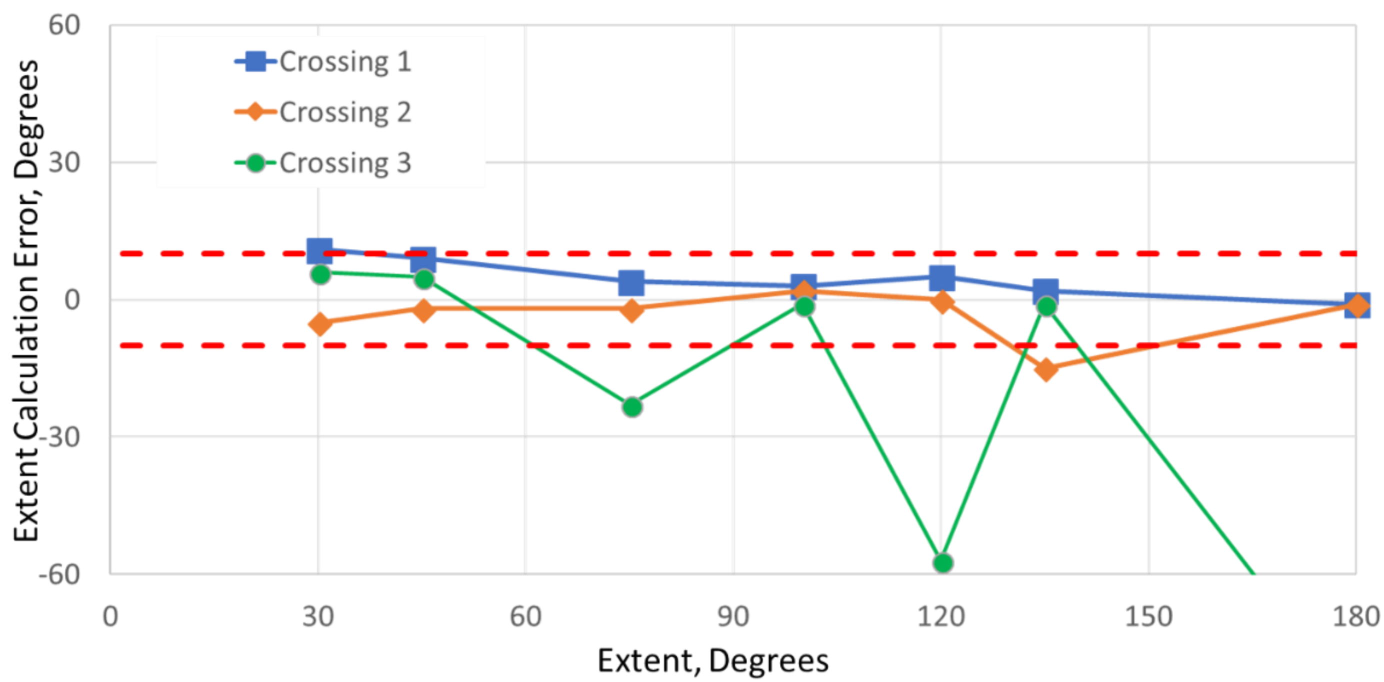

Figure 36 – Extent Calculation Error for 3 Crossing Speeds.

Table 18 – Example Intensity Calculation from NSMS Measurements.

Blade	Adj Amp Mils P-P	EO Scalar (eq2)	Intensity (Amp/Scalar)
1E	259.2	1.273	203.5
2E	2.9	0.011	263.7
3E	77.6	0.424	182.9
4E	1.4	0.011	126.0

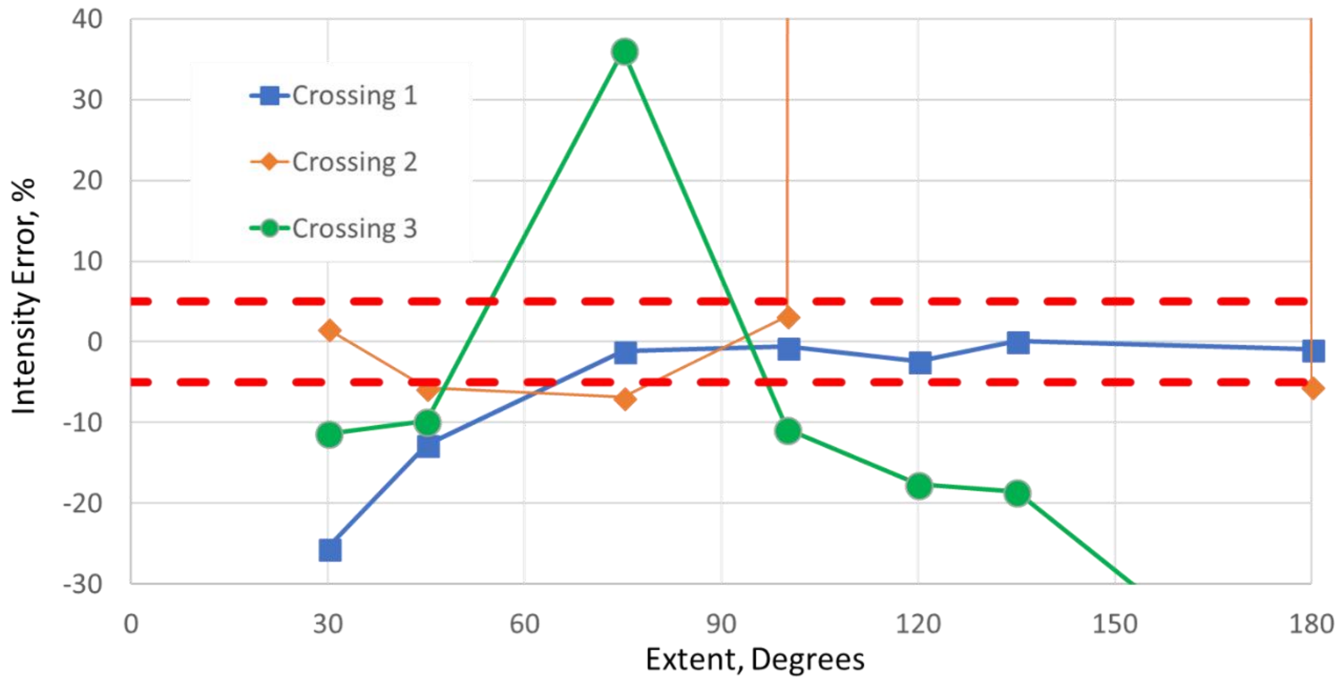

Figure 37 – Intensity Error for Three Different Resonant Crossings.

Table 19 – Resonant Crossing for Modified Mistuned Rotor

Resonant Crossing #	Rotor Speed, RPM	44 Hz Blade EO	88 Hz Blade EO	132 Hz Blade EO	66 Hs Blade EO	99 Hz Blade EO	59 Hz Blade EO
1	2640	1E	2E	3E	NA	NA	NA
2	1980	NA	NA	4E	2E	3E	NA
3	1760	NA	3E	NA	NA	NA	2E
4	1320	2E	4E	6E	3E	NA	NA

VITA

Stephen Andrew Arnold was born in Winchester, Tennessee in 1965, to parents Bill and Jane Arnold. He is the youngest of four brothers, the others being John, David, and Jim. After graduating from Franklin County High School in 1983, Stephen attended the University of Tennessee at Knoxville. He received his Bachelor of Science Degree in Mechanical Engineering from UTK in 1988. In June of 1988, Steve began work at Arnold Engineering Development Center (AEDC) for the operating contractor Sverdrup, Inc. His work at AEDC involved the analysis and evaluation of turbine engine tests conducted in the altitude simulation test chambers of the Engine Test Facility (ETF). Much of the work Steve was involved with concentrated on structural and aeromechanical tests. Steve married Kimberly Renee Wells, an elementary education teacher, in 1994. Their daughter Katherine was born in 1995, and their second daughter Lauren was born in 1998. Steve worked for Experimental Design and Analysis Solutions (EDAS) Incorporated from 2006 until 2010. During his time with EDAS, Steve worked as principal investigator on a Small Business Innovative Research (SBIR) project to integrate measurements acquired with strain gages and Non-contact Stress Measurement System (NSMS) using a Finite Element Model (FEM). In 2010 Steve returned to AEDC to serve as a Senior Test Analyst with Aerospace Testing Alliance (ATA). In 2016, Steve became the Lead Test Analyst for QuantiTech Inc., an Advise and Assist contractor at AEDC. In 2018, Steve was hired by the United States Air Force to serve as Technical Advisor in ETF.